Geoderma 455 (2025) 117216

Contents lists available at ScienceDirect

Geoderma

journal homepage: www.elsevier.com/locate/geoderma

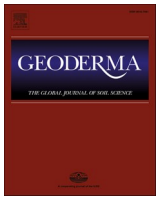

Digital mapping of peat thickness and extent in Finland using remote sensing and machine learning

Jonne Pohjankukka [a,*], Timo A. Räsänen [a], Timo P. Pitkänen [a], Arttu Kivimäki [b], Ville Mäkinen [b], Tapio Väänänen [c], Jouni Lerssi [c], Aura Salmivaara [a], Maarit Middleton [d]

[a] Natural Resources Institute Finland (Luke), Latokartanonkaari 9, P.O. Box 2, 00790 HELSINKI, Finland
[b] Finnish Geospatial Research Institute FGI, National Land Survey of Finland, Vuorimiehentie 5, P.O. Box 84, 02150 ESPOO, Finland
[c] Geological Survey of Finland (GTK), Viestikatu 7 A, P.O. Box 1237, 70211 KUOPIO, Finland
[d] Geological Survey of Finland (GTK), Lähteentie 2, P.O. Box 77, 96101 ROVANIEMI, Finland

ARTICLE INFO

Handling Editor: B. Minasny

Keywords:
Digital soil mapping
Peatland
Peat thickness
Remote sensing
Machine learning
Feature selection
Uncertainty quantification
Nation-wide dataset

ABSTRACT

Accurate data on peat extent and thickness is essential for managing drained peatlands and reducing greenhouse gas emissions. Machine learning-based digital soil mapping offers an effective approach for large-scale peat occurrence prediction. In this study, we present a workflow for producing peat occurrence maps for the whole of Finland. For this, we used random forest classification to map areas with peat thicknesses of $\geq$ 10 cm, $\geq$30 cm, $\geq$40 cm, and $>$ 60 cm. The input data consisted of 3.5 million point observations and 188 feature rasters from various sources. We carefully split the reference data into training and test sets, allowing for independent and robust model validation. Feature selection included an initial screening for multicollinearity using correlation-based feature pruning, followed by final selection using a genetic algorithm. Feature importance was evaluated using permutation importance and SHAP values. The resulting models utilized 26–33 features, achieving overall accuracies and F1-scores between 86–95 % and 0.82–0.95, respectively. The most important features included soil wetness indices, terrain roughness indices, and natural gamma radiation. Additionally, we provided an approach for evaluating spatial prediction uncertainty based on the models' internal prediction agreement. Compared to existing superficial deposit maps, our peat predictions significantly improve the spatial detail of peatlands at the national level, offering new opportunities for land use planning and emission mitigation. Our exceptionally comprehensive approach is broadly applicable, offering new insights into optimizing machine learning-based digital peatland mapping, particularly through refining feature selection to account for local conditions and enhance prediction accuracy.

1. Introduction

Peatlands are terrestrial wetland ecosystems where waterlogged conditions prevent peatland vegetation from fully decomposing, leading to the accumulation of peat (IPS, 2024). The definitions of 'peatland' and 'peat' also vary across climatic regions and often within a single country depending on the context in which they are used (Bruneau & Johnson, 2014; Poggio et al., 2019; Minasny et al., 2024). Covering nearly 3 % of the world's land area, peatlands are increasingly threatened, with 12 % degraded by drainage and land-use changes (e.g., UNEP, 2022; Fluet-Chouinard et al., 2023). When drained, peatlands become significant sources of greenhouse gases due to peat decomposition (IPCC 2019; Evans et al., 2021; Fluet-Chouinard et al., 2023) and they also contribute to water quality degradation. In Finland, where peatlands cover 30 % of the land area (304 000 km^2, Statistics Finland, 2025), nearly half are drained for forestry and agriculture.

Efforts to mitigate the emissions from drained peatlands are often hindered by the lack of accurate data on peatland distribution and thickness. More detailed information on peat soils would also benefit land use planning, carbon stock inventorying and terrain trafficability forecasting. Traditionally, peatlands have been delineated using aerial photographs, airborne radiometric and electromagnetic surveys, and

* Corresponding author.
E-mail addresses: jonne.pohjankukka@luke.fi (J. Pohjankukka), timo.rasanen@luke.fi (T.A. Räsänen), timo.p.pitkanen@luke.fi (T.P. Pitkänen), arttu.kivimaki@maanmittauslaitos.fi (A. Kivimäki), ville.p.makinen@nls.fi (V. Mäkinen), tapio.vaananen@gtk.fi (T. Väänänen), jouni.lerssi@gtk.fi (J. Lerssi), aura.salmivaara@luke.fi (A. Salmivaara), maarit.middleton@gtk.fi (M. Middleton).

https://doi.org/10.1016/j.geoderma.2025.117216
Received 19 November 2024; Received in revised form 7 February 2025; Accepted 10 February 2025
Available online 17 February 2025

field methods such as augering with a peat sampler and surveys with a ground-penetrating radar (Laatikainen et al., 2011; Minasny et al., 2019; 2024). National-scale GIS peatland maps compiled with these traditional mapping techniques are commonly available (e.g. GTK, 2010; Lilja et al., 2017; NLS, 2024). Although the traditional techniques for peat thickness measurements provide accurate maps and their depth range is to the bottom of the peat sediment layer, they are inefficient for national scale mapping.

Recent research has focused on mapping peatlands driven by the need for carbon neutrality (UN, 1997; Minasny et al., 2019; 2024; EU, 2021). Global and European datasets, such as the Global Peatland M ap 2.0 (minimum mapping unit: 1 km x 1 km; UNEP, 2021), Peat-ML (5 arcmin, Melton et al., 2022), and the Peatland Map of Europe (50 ha, Tanneberger et al., 2017). However, all existing datasets lack the spatial and thematic detail needed for effective emission mitigation. They are usually unable to show peat extent and thickness at the level of agricultural field parcels or forest compartments which is required for implementing potential future policies. Also, existing maps lack information on the thin peat layers that has importance for the land use sector e.g., when recognizing the agricultural field parcels on organic soils and conducting greenhouse gas inventory of drained peatlands.

Digital soil mapping (DSM) has proven to be a cost-effective way to delineate peatlands from mineral soils (Aitkenhead, 2017; Hird et al., 2017; DeLancey et al., 2019; Minasny et al., 2019). DSM commonly utilizes optical and synthetic aperture radar (SAR) satellite data and digital elevation models (DEM). Optical and SAR satellite data have been employed to predict peat soil extent (Poggio et al., 2019). Digital elevation models contain indirectly valuable information about peatland presence and soil formation process occurring due to slow decomposition rates of organic material in anaerobic conditions and consequent accumulation and distribution of organic matter at topographic lows (Jenny, 1994; Minasny et al., 2019; Ågren et al., 2022). High-resolution DEMs can identify microtopographic features such as flarks, hummocks, and pools, which are characteristic of peatland vegetation (Korpela et al., 2020). Indices based on DEM such as depth-to-water index (DTW; Murphy et al., 2007; 2008; Ågren et al., 2014) reveal moisture gradients in the landscape. They have proven useful, either alone or with other spatial data, for mapping peat extent and thickness (Lidberg et al., 2020; Aitkenhead, 2017; Ågren et al., 2022; Rimondini et al., 2023).

Another significant source of information used for DSM of peat thickness are airborne geophysical data. Radiometric and electromagnetic data from low-altitude airborne surveys, such as those reported by Airo et al. (2014) and O'Leary et al. (2022), have particularly demonstrated effective in predicting peat thickness (Minasny et al., 2019, O'Leary et al. 2025). Radiometric data has shown significant capability (Lahti and Häme, 1992; Gatis et al., 2019; Siemon et al., 2020; O'Leary et al., 2022; Lerssi et al., 2023, O'Leary et al. 2025) because natural radiation of bedrock and Quaternary sediments is attenuated by the physical properties of peat. The high ground water table in peatlands leads to full saturation and increased bulk density, resulting in low radiation from peatlands. Water layer with a thickness of 60–70 cm is reported to absorb gamma radiation completely (Davisson, 1968; Endrestøl, 1980; Beamish, 2015). Electromagnetic data, on the other hand, has been utilized for predicting peat thicknesses of several meters (Puranen et al., 1999; Silvestri et al., 2019; Siemon et al., 2020; Lerssi et al., 2023). At 3.1 kHz, the in-phase component reflects good conductors like bedrock, while the out-of-phase component highlights weakly conductive sediments like saturated organic layers (Puranen et al., 1999; Suppala et al., 2005; Lerssi et al., 2023).

However, all the abovementioned data have also some limitations when used in modeling of peat thickness. Optical data have no penetration through vegetation and soil layers, while SAR satellite data have limited penetration. Only L-band SAR (1–2 GHz) can partially penetrate vegetation and reach top sediment layers (~10 cm). LiDAR DEM-derived topographic indices offer only indirect information on peat accumulation in lowlands, lacking details on the physical properties of sediment cover (Jenny, 1994; Minasny et al., 2019; Ågren et al., 2022). Airborne gamma radiation data provide physical–chemical properties of subsurface sediments (IAEA, 1991; Beamish, 2015), but the relationship between radiation and peat thickness is affected by factors like geological material, drainage, sediment mixing, and fertilizers (Schnug et al., 1996). Furthermore, its spatial resolution depends on flight line separation, leading to significant scatter in the relationship between peat thickness and radiation intensity (Lerssi et al., 2023). Electromagnetic data, however, can penetrate several tens of meters but its vertical resolution is limited even when the highest frequencies are used (Suppala et al., 2005).

Because of the deficiencies in remote sensing (RS) and geophysical data, successful DSM of peat extent and thickness mapping requires multi-source data (Aitkenhead, 2017; Minasny et al., 2019; Ågren et al., 2022; Rimondini et al., 2023). Yet, no studies exist aggregating all commonly available weak predictors for optimal peat thickness modeling. Furthermore, no examples of utilizing temporal soil moisture differences between peat and mineral soils for delineating the mineral and peat soils are available in the literature. Peat maintains higher moisture than mineral soils during the growing season, even throughout drought periods (Päivänen, 1973). This phenomenon could be captured with optical and SAR data. Auxiliary information could also be received from geomorphological data, such as ancient shorelines, which may provide insights into peatland formation over the Quaternary period (Mäkilä et al., 2013; Bhiry et al., 2007). In Finland, peat thickness is linked to the Baltic Sea's water level changes after the last glaciation (Eronen, 1991; Kakkuri & Virkki, 2004).

Aggregation of a wide range input raster data from multiple sources for machine learning (ML) results in a high dimensional feature set, i.e. a raster data stack with tens or hundreds of predictor data layers. To effectively conduct DSM, careful feature evaluation and robust model validation are thus essential. In the context of ML, selecting the optimal combination of features (or datasets) is crucial for accurately modeling the response variable. While a large feature set can be advantageous, it may also introduce challenges, such as noise from irrelevant features and skewed analyses due to feature correlations (Abu-Mostafa et al., 2012; Chen et al., 2020). Feature selection techniques, such as genetic algorithms, forward selection and principal component analysis, are commonly used to search for/determine the optimal feature subsets (Wold et al., 1987). Equally important is model validation, typically done through data splitting and cross-validation techniques. However, reviews highlight that fully independent, model-free validations are rare. Additionally, prediction uncertainty is often overlooked, leading to overfitting, suboptimal predictions, and limitations in the interpretation of the results (Wadoux et al., 2020; Minasny et al., 2019). These issues are particularly problematic when model outputs are used for practical decision-making and management.

The goal of this study was to enhance large-scale peat extent and thickness mapping by integrating a rarely employed, comprehensive DSM framework while producing improved peatland data for Finland. The approach combined exceptionally large soil observation dataset with diverse remote sensing (RS) and GIS data using machine learning (ML). It incorporated advanced feature selection and evaluation and underwent robust independent model validation. Additionally, it provided an estimate of the spatial distribution of prediction reliability. It was hypothesized that this DSM approach enhances the spatial and thematic detail of existing nationwide data on peat extent and thickness within the top 60 cm of the ground.

The soil observations used for model training and independent testing were collected from various sources, totaling 3.5 million point observations. Such a large and spatially uncorrelated training and testing dataset has not been previously reported for DSM of peat thickness. This enabled an independent, representative, and unbiased performance estimation of the country-wide models, covering all land use classes in Finland. The RS and GIS data comprised 188 spatial features

from a range of sources, resulting in a previously unreported set of predictor variables. These included Sentinel-2 and Sentinel-1 satellite RS data, airborne LiDAR DEM, airborne geophysical and geomorphological data, and their various derivatives.

We introduced an advanced feature selection approach to identify the most relevant predictors for ML predictions from a diverse geospatial dataset. Feature selection involved an initial multicollinearity screening using correlation-based feature pruning, followed by a final selection using a genetic algorithm. The approach grouped correlated features similarly to hierarchical clustering (Nielsen, 2016), reducing the impact of redundant information in feature evaluation. A genetic algorithm was chosen for its efficiency in navigating complex, high-dimensional search spaces, as exhaustive feature selection was infeasible. The importance of the selected features was then assessed using permutation importance (PI, Breiman, 2001) and SHAP (Shapley additive explanations; Štrumbelj & Kononenko, 2014; Padarian et al., 2020).

Peat thickness prediction was approached as a binary classification task, with independent ML models developed for four peat thickness categories: ≥10 cm, ≥30 cm, ≥40 cm, and > 60 cm. Random forest (RF) was chosen as the modeling method for its robustness and effectiveness in handling complex classification problems (Breiman, 2001), as well as its proven efficiency in peatland prediction (Minasny et al., 2019). The spatial distribution of RF prediction reliability was assessed based on the model's internal agreement across individual regression trees. The efficacy of the proposed DSM approach was further evaluated by comparing it to the Superficial Deposit 1:200,000 map, currently the only nationwide peat thickness dataset available.

The peat thickness classes (≥10 cm, ≥30 cm, ≥40 cm, and > 60 cm) were selected to align with national and international soil classification systems used to define 'peatlands,' 'organic soils,' and 'Histosols.' 'Peat' was classified based on existing criteria, requiring a minimum organic carbon content of 20 %, approximately equivalent to 40 % organic matter (NLS, 2024; GTK, 2010, 2015; IUSS Working Group WRB, 2022; IPCC, 2019). Soils with less than 20 % organic carbon and a peat layer thinner than 10 cm were classified as non-peatlands and are referred to hereafter as 'mineral soil.' These definitions ensure data compatibility with existing land use planning, management, and monitoring efforts, including the national greenhouse gas inventory.

2. Materials and methods

2.1. Study area

Finland, located in the boreal zone of Europe, is characterized by gently undulating topography with approximately 75 % of the area situated within 200 m above sea level (Alalammi, 1986). Approximately 30 % of the country is covered by peatlands, which most commonly occur in northern Finland and along the coastal region of Gulf of Bothnia (Fig. 1; Syke, 2024a; Ruuhijärvi, 1988). Peatlands are divided into two main ecological types; raised bogs dominate in the hemiboreal and southern boreal zones and *aapa* mires in the middle and northern boreal zones (Eurola et al., 1994). The thickness of peat deposits varies up to 10.2 m with mean thickness of 1.4 m (Virtanen et al., 2003). About 55 % of peatlands have been drained for forestry and agriculture since 1950′s (Turunen & Valpola, 2020).

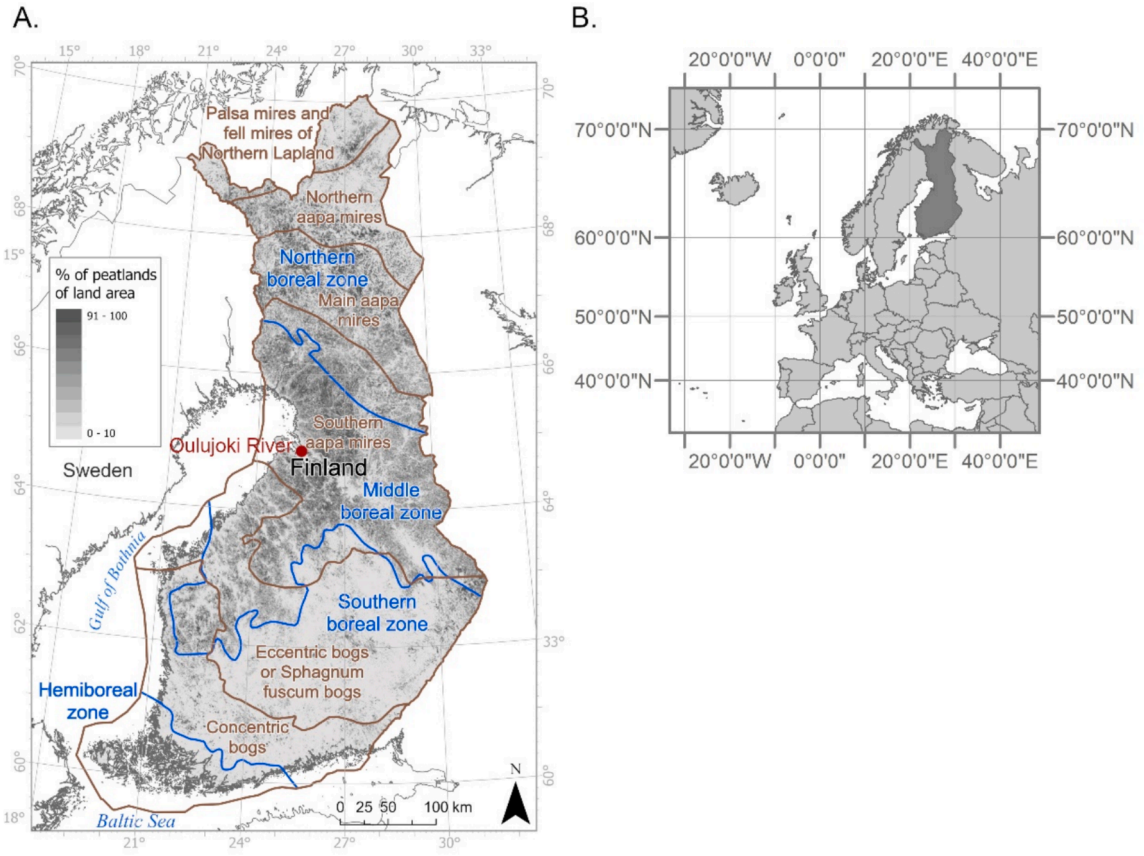

Fig. 1. A. Main mire, i.e. peatland, vegetation zones (brown) and climate driven forest vegetation zones (blue) in Finland underlined by the density of peatlands, and B. Location of Finland in Europe (© Syke, 2024a, 2024b; CC BY 4.0; Country borders ©Esri Living Atlas, 2024; Farahnakian et al., in prep.). Location of Oulujoki River sample area is shown in tile A with red dot. (For interpretation of the references to color in this figure legend, the reader is referred to the web version of this article.)

2.2. 2.2 Reference data for model training and testing

The reference data utilized for training and independent testing of the ML models consisted of peat thickness measurements (48.3 %, see description in para. 2.2.1), surface soil observations (15.6 %, see para. 2.2.2) and generated pseudo-observations (36.1 %, see para. 2.2.3). The data were collected from national and European sources. A reference year to represent the peat thickness status was set to 2022 and the measurements and observations, which were collected in 1980–2023, where age-corrected to match this year. The reference data are introduced in detail in the following sections and summarized in Table 1.

2.2.1. Peat thickness measurements

Peat thickness measurements, collected over the past 80 years by the Geological Survey of Finland (GTK, 2017a, 2017b, 2018), Natural Resources Institute Finland (Korhonen et al., 2021), and smaller surveys, comprise 48 % of the reference data (Table 1). A frequency histogram of all observations is shown in Fig. A2 (A ppendix A). Measurements were taken using various peat samplers, such as hand-held Russian (Macanlay) corers, which also extracted samples down to the mineral soil. Soil texture was typically assessed by trained personnel using sensory assessment following the Finnish RT classification system (Pohjarakennuksen normit, 1964) and protocols (Lappalainen et al., 1984; Haavisto, 1983; Metsäntutkimuslaitos, 2009). In a few cases, peat was identified via laboratory analysis by an organic matter content of $\geq$ 40 % ($\approx$ 20 % organic carbon; IUSS Working Group WRB, 2022).

In this study, peat thickness measurements on agricultural lands were age-corrected to the 2022 reference year to account for peat layer reduction from decomposition (due to drainage) and soil compaction from agricultural activities (Evans et al., 2021). An average reduction rate of 1.2 cm per year was applied (Räsänen et al., 2023). The average (median) time between measurement and reference year was 16 (12) years, resulting in an average (median) correction of −19.4 cm (−14.4 cm). This correction affected 3 % of the peat observations used in modeling. Measurements from other intensively managed areas, like peat extraction sites, were excluded due to insufficient data on peat thickness changes.

In $<$ 1.5 % of cases where peat observations were incomplete and the sampler did not reach the peat layer's bottom, measurements were included in predictions only if the depth met the threshold for the predicted peat thickness class. For instance, a 20 cm sampling depth was used to predict the $\geq$ 10 cm class but excluded from the predictions for $\geq$ 30 cm, $\geq$ 40 cm, and $>$ 60 cm classes.

2.2.1.1. Surface soil observations and samples. The surface soil observations were comprised of data collected by Geological Survey of Finland (GTK, 2018), Natural Resources Institute Finland (Korhonen et al., 2021), ESDAC (Fernandez-Ugalde et al., 2022; Jones et al., 2020; Tóth et al., 2013), and individual research projects totaling of 16 % of the training data (Table 1). These observations were based on soil probing and sensory assessment of the soil type, and on laboratory analysis of the soil samples (sampling depth $\leq$ 30 cm). In these data sets, peat is defined as having organic matter content $\geq$ 40 % ($\approx$ 20 % organic carbon; IUSS Working Group WRB, 2022).

2.2.1.2. Pseudo-observations. Compilation of the observations (Sections 2.2.1-2.2.2) resulted in a dataset which was dominated (77.0 %) by peat soil observations (Table 1). Using such data to train ML models contains the risk that the models become biased and tend to over-predict. Training data needed to be balanced by generating pseudo-observations on 'mineral soils' with no peat layer of any thickness present. The generation was based on Topographic database (NLS, 2024) and Superficial Deposits Maps (1:20,000, 1:50,000, 1:100,000 and 1:200,000) (GTK, 2010, 2015, 2015b). The Topographic database was first used to exclude areas which are not on mineral soils (e.g., surface waters, peatlands, wetlands, built-in areas, roads, earth fill sites). They were buffered outward with arbitrary distances of 25 and 50 m. Then the buffered vector layers were converted into binary raster layers and combined by multiplying them all together, resulting in mineral soil areas. This raster was then converted back into a polygon and further buffered inward by 25 m to ensure that all generated random points would fall only within mineral soils. Then, altogether 1.3 million pseudo-observations were generated randomly by the Standardize Field and Create Random Points tools (Esri's ArcGIS Pro version 3.0.x and later versions) on the remaining potential mineral soil areas. They were further filtered using the Superficial Deposits Maps, such that the generated observations located at mud or peat soils, earth fill sites and unmapped areas were excluded. This resulted in 1,282,781 mineral soil pseudo-observations, comprising 36 % of the final reference data (Table 1).

2.2.1.3. Training and test partitioning of reference data. After data preparations, all observations were combined into a single reference data totaling 3,552,286 independent data entries covering various land cover and use types (Table 1). The highest density of the reference data was on the west coast of the country, where peatlands most frequently occur and therefore are most inventoried (Fig. A1 in A ppendix A). The agricultural lands had 97,309 data points, of which 53 % were peat observations and $<$ 4 % pseudo-observations.

The compiled reference data were then partitioned into training (70 %) and independent test data (30 %) sets with similar statistical and spatial distributions. As is common in ML, parts of the training set are used as validation sets (e.g. in cross-validation) which are used for optimizing, e.g., the hyperparameters of the model. After the model has been fully calibrated a final unbiased performance estimate is produced using the test set.

The initial observations were spatially unevenly distributed and often clustered into small areas resulting in spatial autocorrelation between the data locations, which would inflate the prediction accuracies of the RF models (see e.g., Karasiak et al., 2022). Thus, we adopted a partitioning strategy using square tiles as sampling units. First, the country was divided into a 10 km $\times$ 10 km grid, containing 3,784 with minimum of one observation. Then, these tiles were divided into a candidate training and test set pair by sampling them in random order

Table 1
Summary of the reference data used for training and testing the random forest models.

Data	Description	Soil observations	Peat soil observations	Source
Peat thickness measurements	Peat layer thickness measurements using various soil augers. Soil type identification mainly by visual means but also by laboratory analysis.	1,715,441	1,715,441	GTK (2017a, 2017b, 2018), Korhonen et al. (2021)
Surface soil observations	Observations of surface soil with soil type identification based on soil probing, visual identification, and laboratory analysis.	554,420	33,139	Fernandez-Ugalde et al., 2022; Heikkinen et al., 2021; Korhonen et al., 2021; Soinne et al., 2022; Tóth et al., 2013; GTK, 2018; Jones et al., 2020
Pseudo-observations	Generated pseudo-mineral (non-peat) soil observations based on soil cover and soil maps.	1,282,781	–	Generated in this work
Total		3,552,286	1,748,580	

until 30 % of the observations were selected. The statistical and spatial similarity of the two sets was then quantified by classifying peat thickness, x-coordinates, y-coordinates, and origins (observed or generated) of the observations into suitable classes and calculating the sum of their squared proportional differences between the sets. 1,000 candidate pairs of tiles were generated using this method. Finally, the training and test sets applied in the study were selected among the candidates based on the smallest difference sum (see Fig. A1c in A ppendix A). Further, those test set observations which were close to the edges of the polygons and were located within 200 m away from any training set observation (n = 27,554), were removed. This minimum distance was determined by the range of spatial autocorrelation, using a semivariogram derived from the peat thickness measurements (Fig. A3 in A ppendix A.).

2.3. Predictor data

Four types of spatial data were used as spatial features in the prediction of peatlands: airborne geophysical survey data, airborne LiDAR-derived DEM data, optical and SAR satellite data, and geomorphological data. These data are introduced in detail in the following sections and summarized in Table 2.

2.3.0.1. Airborne geophysical survey data

The national airborne geophysical low altitude survey program, described in detail by Airo (2005), was carried out during 1973–2007 covering the entire country of Finland. The nominal flight altitude was 40 m and flight line spacing 200 m. Sample distance along the survey line was 6–50 m depending on the registration rate. The choice of standard flight directions north–south and east–west was made to suit the main geological trends of each flight area. The resulting gridded data of 50 m × 50 m cell size contains electromagnetic out-of-phase (imaginary), in-phase (real), and apparent resistivity, and the natural radiometric radiation of potassium (^{40}K), thorium (^{232}Th), uranium (^{238}U), and total count (UR) data. The electromagnetic coil system was frequency domain coplanar using frequency of 3.1 kHz (Suppala et al., 2005). In this research we used radiometric potassium (^{40}K) and thorium (^{232}Th) window data and their ratio, as well as in-phase and out-of-phase components of electromagnetic field and their ratio (Table 2).

2.3.0.2. Airborne LiDAR-derived digital elevation model (DEM) data

DEM-based feature included Depth-to-Water (DTW) index and a set of geomorphometric indices. All these were based on the same airborne LiDAR-derived DEM with 2 m × 2 m resolution covering the whole of the country (NLS, 2020).

DTW is based on cost surface analysis calculating the least-cost pathway to the nearest point in stream network that is defined based on varying flow accumulation thresholds. Low DTW index values indicate wet areas. Here we used the DTW index with a 2 ha threshold (Salmivaara, 2023) corresponding to average hydrological conditions and representing slightly wetter conditions than the 4 ha DTW index that has been suggested for the end-of-summer conditions (Ågren et al., 2014).

The geomorphometric indices were used to quantifying local topographic variation between the peat and mineral soils. First, a set of potential indicators was identified based on earlier studies (Table 2), and a diverse subset of soil observations was selected to test their performance (Ågren et al., 2021; Langlois et al., 2017; Richardson and Millard, 2018; Grohmann et al., 2010; Riley et al., 1999; Poggio et al., 2019; Aitkenhead, 2016; Lindsay et al., 2019). Geomorphometric index values were calculated in variable window sizes (i.e., blocks of DEM pixels surrounding the target pixel) using WhiteboxTools (Lindsay, 2016). For some indices, calculation was limited to window sizes of 3 × 3 or 5 × 5 pixels. For the rest of the indices, multiple window sizes between 3 × 3 and 31 × 31 were calculated as the optimal size was unknown. The applicability of the calculated indices for modelling of peat thickness was initially assessed by comparing their value distributions between

Table 2
Summary of the spatial feature data and their short names used in text for peat thickness and extent modelling. The modelling was performed at 50 m × 50 m grid resolution and all feature data were prepared or converted to this resolution.

Spatial feature names in text	Description	Source, data reference
Airborne geophysical survey data		
AR K	Airborne radiometric (AR) data. Potassium radiation (^{40}K) component measured with gamma spectrometry. measurements	Geological Survey of Finland (GTK), Airo at al. (2005).
AR Th	Airborne radiometric (AR) data. Thorium radiation (^{232}Th) component measured with gamma spectrometry measurements.	
AR K/Th	Airborne radiometric data. The ratio of ptotassium (^{40}K) and Thorium (^{232}Th) radiation.	
AEM Re	Airborne electromagnetic (AEM) data. The In-phase (real) component of electromagnetic field.	
AEM Im	Airborne electromagnetic (AEM) data. The out-of-phase (imaginary) component of electromagnetic field.	
AEM Re/Im	Airborne electromagnetic data (AEM). The ratio of the In-phase (real) and out-of-phase (imaginary) component.	
Airborne LiDAR-derived Digital Elevation Model (DEM) data		
DTW 2 ha	Depth-to-Water, a measure for wetness conditions of the soil based on topography (Murphy et al 2007; 2008).	Salmivaara (2023)
DEM SAR 3 × 3 mean, std	Surface area ratio: Ratio between the surface area and planar area of the window; value of 1 is perfectly flat, otherwise gaining larger values; Grohmann et al. (2010).	Calculated in this work using DEM data in 2 m resolution followed by aggregating the results into 50 m pixel resolution as mean and standard deviation statistics. Short names include the window size(s) applied in the RF modelling.
DEM var 31 × 31 mean, std	DEM variation: Standard deviation of the DEM elevation using 31 × 31 window size; Ågren et al. (2021), Grohmann et al. (2010).	
DEM slope var 31 × 31 mean, std	Slope variation: Standard deviation of the slope using 31 × 31 window size; Ågren et al. (2021), Grohmann et al. (2010).	
DEM CVA 5 × 5 mean, std DEM CVA 11 × 11 mean, std DEM CVA 31 × 31 mean, std	Circular variance of aspect: Measure of how variable aspect is within the window of sizes 5 × 5, 11 × 11, and 31 × 31; flat surfaces gain a value of 0 and rough surfaces approach 1; Ågren et al. (2021), Grohmann et al. (2010), Lindsay et al. (2019).	
Satellite data		
NDMI	Normalised Difference Moisture Index, a measure for moisture levels in vegetation (Gao, 1996).	Mosaic calculated in this work. Original Images from Sentinel-2 L2A (ESA 2024a).
NDVI	Normalised Difference Vegetation Index, a measure for density of vegetation (Rouse et al., 1973).	
EVI2	Enhanced Vegetation Index 2, a measure for density of vegetation (Jian et al., 2008).	
NBR	Normalized Burn Ratio, a measure for burnt areas (Key and Benson, 1999).	

(continued on next page)

Table 2 (*continued*)

Spatial feature names in text	Description	Source, data reference
kNDVI	Kernel Normalised Difference Vegetation Index, a measure for density of vegetation (Camps-Valls et al., 2021).	
NDSI	Normalised Difference Snow Index, a measure for presence of snow (Riggs et al., 1994).	
SAVI	Soil-Adjusted Vegetation Index, a measure for density of vegetation with adjustment for soil related effects (Huete, 1988).	
SCI	Soil-color Index, a measure for soil color (e.g., Poggio et al., 2019).	
SM	Soil Moisture Index, a measure for soil moisture (Dupigny-Giroux and Lewis, 1999).	
TCTb	Tasseled-Cap Transformation Brightness, a measure of brightness for the ground (Kauth and Thomas, 1976; Shi and Xu, 2019).	
TCTg	Tasseled-Cap Transformation Greenness, a measure of greenness for the vegetation (Kauth and Thomas, 1976; Shi and Xu, 2019).	
TCTw	Tasseled-Cap Transformation Wetness, a measure of interactions of soil and canopy moisture (Kauth and Thomas, 1976; Shi and Xu, 2019).	
SAR VV	Synthetic Aperture Radar vertical–vertical polarization intensity.	Mosaics from FMI (2020) and original images from Sentinel-1 (ESA 2024b).
SAR VH	Synthetic Aperture Radar vertical-horizontal polarization intensity.	
SAR ratio	SAR VV-HH polarisation ratio (VH-VV)/(VH + VV).	
Geomorphological data		
Shoreline	Sub- and supra-aquatic areas as described by the ancient shorelines during the melting period of the last ice age.	Geological Survey of Finland (2013)

peat vs. mineral soil classes visually using box-plot diagrams. Indices with no apparent discrimination ability between the classes (i.e., with highly overlapping distributions) were discarded at this phase. The remaining indices included DEM variation, surface area ratio, ruggedness index, slope, slope variation, and circular variance of aspect which resulted in a set of 18 features.

2.3.0.3. *Satellite data*

The satellite data included several mosaics that were based on optical data from Sentinel-2 (ESA, 2024a) and synthetic aperture radar (SAR) data from Sentinel-1 (ESA, 2024b). The selection of optical indices and SAR product was based on a literature review to include features that have been previously demonstrated effective in the DSM of peatlands. Selected indices and SAR products are listed in Table 2, and the formulas for optical indices are provided in T able A1 in A ppendix A.

Optical mosaics were created from Sentinel-2 L2A products from summer season 2021 (Copernicus Open Access Hub, closed in October 2023). For each Sentinel-2 tile, images for each band (9 bands 490 – 2190 nm) were created with sen2mosaic tool (sen2mosaic, 2017) with 30-day time windows (T able A2 In A ppendix A), and spectral ndices were calculated with resulting cloudless images. After calculation, index tiles were combined into mosaics covering the country, resulting in a set of 156 features. The original spatial resolutions of mosaics were 10 m × 10 m or 20 m x 20 m, depending on the bands required for index calculation.

Sentinel-1 SAR mosaics were based on 11-day mosaic products provided by the Finnish Meteorological Institute (FMI, 2020) from the summer season 2021. The mosaics were created from Ground Range Detected (GRD) products with the IW sensor mode and a descending orbit. Due to spatial gaps in data coverage, the original mosaics were averaged over time into four mosaics with approximately 50-day time windows (T able A2 in A ppendix A) to have data values in each pixel. This resulted in a total of 12 SAR features. The original spatial resolution of SAR mosaics was 20 m × 20 m.

2.3.0.4. *Geomorphological data*

The geomorphological data consisted of ancient shoreline map data (vector data, polygons), describing the sub- and supra-aquatic areas after melting of the Fennoscandian continental glacier during the different phases of the Baltic Sea in Holocene. The data was included because as the glacier melted, the Earth's crust rebounded (Eronen, 1991; Kakkuri and Virkki, 2004), leading to peat formation first in depressions above the highest shore levels (supra-aquatic areas) and later on newly exposed subaqueous lands (Hokkanen, 2005; Mäkilä et al., 2013). Peat accumulated approximately 10,000 years longer in supra-aquatic areas above the highest ancient shorelines which currently lie at about 220 m a.s.l. in northern Finland and at 100 m a.s.l. in south-eastern Finland (see Fig. 1; Tikkanen and Oksanen, 2002). Right along the coast of the Gulf of Bothnia, this process is just beginning. Gridded data of the sub- and supra-aquatic areas was prepared for modeling from Ancient Shorelines data, which is in vector format (GTK, 2013; Table 2).

2.3.0.5. *Final spatial features*

The geophysical radiometric and electromagnetic data have been validated as a key source for peat thickness information (Minasny et al., 2019; Airo et al., 2014; Hyvönen et al., 2005; Virtanen, 1997; Lerssi et al., 2023). Therefore, we used these rasters as they are and transformed the other datasets into the same 50 m x 50 m resolution and alignment. The satellite rasters were resampled using bilinear interpolation and the DTW raster was resampled using mean sampling. For the DEM-derived incides the mean and standard deviation were aggregated from the finer 2 m x 2 m rasters. The geomorphological vector data was rasterized using the center of cell to select the vector feature that decides the value of the cell. Waterbodies were masked out of all feature data. At this stage, 188 spatial features were produced: 6 airborne geophysical, 13 DEM, 156 Sentinel-2, 12 Sentinel-1 derived features, and one geomorphological feature.

To address multicollinearity between the features, the most correlating layers were removed in two phases. The first phase was only performed for geomorphometric indices (Section 2.4.2) using the initial results in 2 m resolution before aggregating them into 50 m grid cells. The Pearson's correlation coefficients were calculated between these features. The coefficient of 0.75 was determined as a maximum threshold value which intended to reduce efficiently multiple window sizes of the same indices, and the elimination was started from the highest correlating pair. For those two features, a separate logistic regression model was built to classify the peat/non-peat observations. The feature with a lower classification performance, based on the Akaike information criterion, was then dropped out. This process continued until no index pair exceeded the threshold correlation coefficient. As a result of this process, surface area ratio (3 × 3), DEM variation (31 × 31), slope variation (31 × 31) and circular variance of aspect (5 × 5, 11 × 11 and 31 × 31) were the remaining features (n = 12), respectively (Table 2). The second phase targeted all the input layers in the final 50 m cell size and intended at decreasing their number prior to modeling. The procedure was like the one used for geomorphometric indices, and maximum Pearson's correlation was set to 0.9 for dropping out only the most similar features. The layers to be removed were determined by their lower performance in classifying the peat/non-peat observations.

This procedure reduced the number of input data layers from 188 to 116. The resulting features cover 99.5 % of the land surface area of Finland. The no-data areas (the pixels for which at least one covariate is missing, < 0.5 %) resulted primarily from the airborne geophysical survey data and DTW index.

2.4. Machine learning methods

2.4.0.1. Modeling process

The overall analysis workflow for prediction of peat extent and thickness is summarized in Fig. 2 and the methodological stages are explained in detail in the following sections. First, we chose a threshold value for the peat thickness and labeled the training and test data into binary classes (0 = below, 1 = above the threshold thickness).

Then, we trained an RF model with the corresponding binary data. The selection of the most appropriate predictor feature data from the set of 116 features was implemented using a genetic algorithm (GA) approach. Stratified 3-fold cross-validation was used to evaluate RF model performance during the training and feature selection procedures. The optimal set of selected spatial features was also evaluated by using the permutation importance method and Shapley values (Štrumbelj and Kononenko, 2014). The former method identifies the most significant feature groups, while the latter examines the impact of individual features on peatland thickness predictions. Also, a regression analysis was conducted between the RF model prediction reliability, quantified as the agreement of the decision trees, and the corresponding prediction accuracy. This approach helps in estimating the expected accuracy of an RF prediction based on its level of agreement.

Finally, the RF model is used to classify the cells for the whole country to either have peat thickness above or below the chosen threshold value. In addition to the binary classification, the model also outputs its internal estimation (probability) of the classification being correct for each cell. These estimates are then compared against an independent out-of-sample test set for measuring the model's prediction performance.

The whole process was repeated independently for four peat thickness threshold values 10 cm, 30 cm, 40 cm, and 60 cm. We refer to these models as RF10, RF30, RF40, and RF60, respectively. All corresponding analyses were implemented using Scikit-learn- (Pedregosa et al., 2011) and SHAP-libraries (Lundberg et al., 2020).

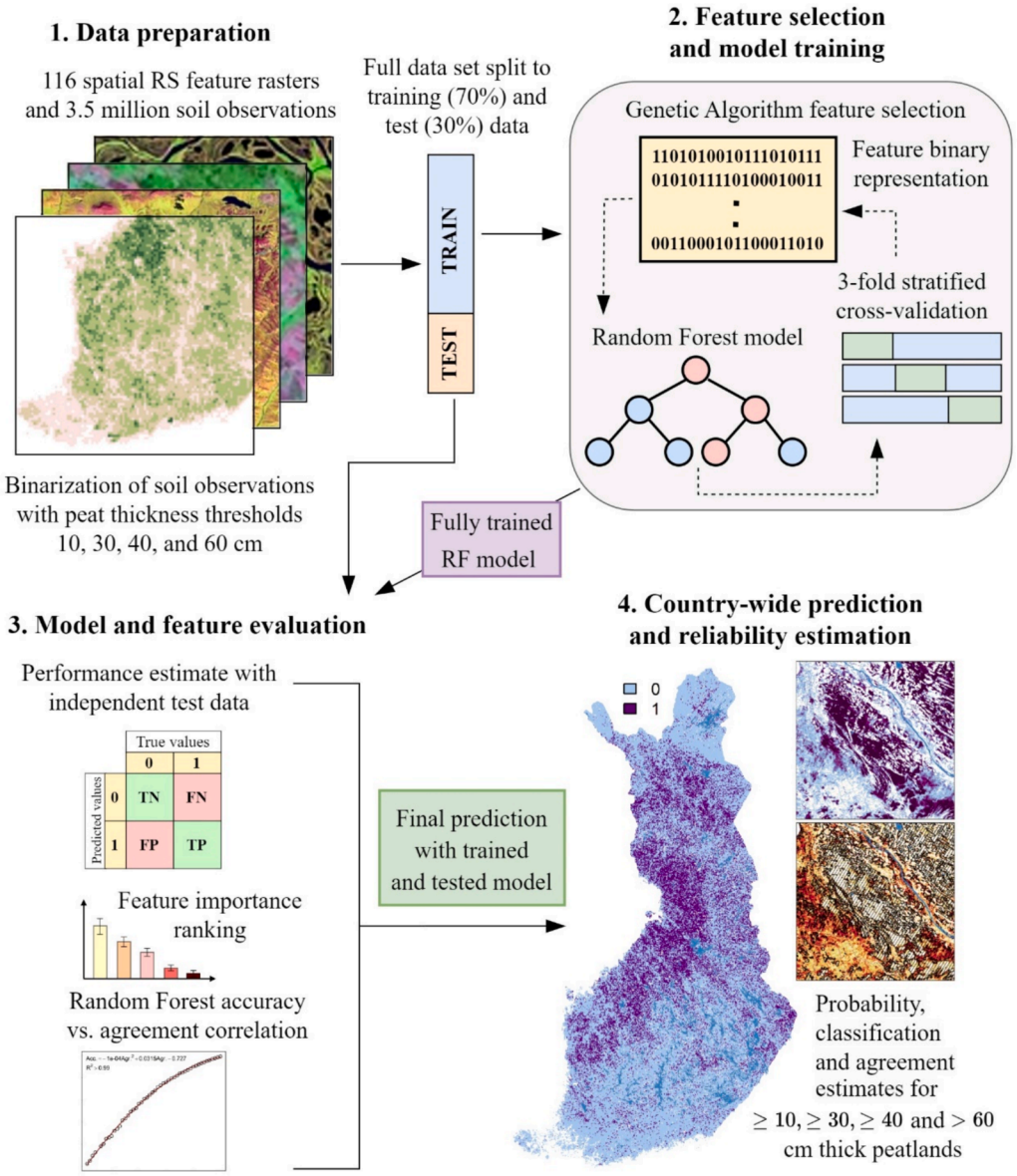

Fig. 2. Peat thickness and extent modeling workflow.

2.4.0.2. Model for peat thickness and extent

2.4.0.2.1. Random forest classifier. Random forest (RF) belongs to a class of ensemble learning methods and is widely used both in classification and regression tasks (Breiman, 2001). RF is a well-established method and has been shown to outperform many other ML models in various contexts (e.g., Fadhurrahman and Saputro, 2022; Uddin et al., 2019; Minasny et al., 2019; Poggio et al., 2019; Rimondini et al., 2023) and ensemble models in general can be shown to have better expected model performance over individual ML models (e.g., Bishop et al., 2023). Our employed binary RF models (RF10, RF30, RF40, RF60), composed of 100 decision trees, were used to generate classifications (0/1), probability and prediction reliability estimates in the corresponding peatland thickness class cases (peat thickness thresholds 10, 30, 40, 60 cm).

2.4.0.2.2. Model prediction reliability. RF also offers a convenient method for assessing prediction reliability by examining the level of agreement amongst the predictions by individual decision trees. Each tree generates its own prediction, allowing for consensus evaluation amongst them. By quantifying the degree of agreement or identifying the maximum level of agreement, one can gain insights on the level of conflict or disagreement within the ensemble. We dealt with binary RF classification models for which the agreement values ranged between 50 and 100. An agreement of 50 corresponds to a case when half of the decision trees classify an observation as a negative class and the other half as a positive class. This corresponds to a maximum entropy (Shannon, 1948) situation for the model. Similarly, the agreement value of 100 corresponds to all decision trees classifying an observation the same way, either to a negative or a positive class. In addition to the peatland prediction maps, we produced corresponding RF tree agreement (i.e., model prediction reliability) maps.

To explore whether the agreement values can provide a meaningful estimate of the prediction reliability, we examined the relationship between the RF agreement and overall accuracy of the RF classification. This was implemented on the training data by first calculating the accuracy value of the RF prediction and regressing it with the corresponding agreement value (50–100). A second order polynomial model was fitted between the agreement and accuracy values for describing the relationship between them. The relationship between the RF agreement and accuracy was studied for all RF models, i.e., RF10, RF30, RF40, and RF60.

2.4.0.3. Feature selection and evaluation

We used the genetic algorithm method to select optimal feature subsets and applied permutation importance and Shapley additive explanations to evaluate the importance of selected features in predicting peatlands using RF. These three methods address related but complementary questions. Genetic algorithm was used to answer which features are optimal for the RF models. After this, the two latter methods were used to analyze how these selected features influence the models' prediction performance, and how their values affect the models' outputs, respectively.

2.4.0.3.1. Genetic algorithm. Genetic algorithms (GA, Sastry et al., 2005) are a class of optimization algorithms inspired by the principles of natural selection and genetics. They belong to the broader category of evolutionary algorithms, which mimic the process of natural selection searching for optimal solutions to complex problems. It maintains a population of potential feature subsets and employs genetic operators, like crossover and mutation, to evolve these subsets towards improved performance. By systematically evaluating and stochastically combining well-performing feature subsets, GA aims to converge towards an optimal or near-optimal solution in the feature space.

In this work, we used GA to optimize the explanatory feature combinations for all RF-models independently. We used the population size of 100 and ran the GA for 50 generations or until the performance of the model did not increase. Cross-over, elite, and mutation probabilities of 49.5 %, 10 % and 1 % were used, respectively.

2.4.0.3.2. Permutation importance. The permutation importance (PI, Breiman, 2001) method is a powerful technique used in ML to evaluate the importance of features in predictive models. It provides insights into which features contribute the most to the predictive performance of the model and helps in identifying influential variables in the dataset. The PI method measures the impact of shuffling or permuting the values of a particular feature on the model performance. If a feature is truly important for the prediction efficiency, shuffling its values should significantly degrade the model performance.

It is well-known that the PI method is sensitive to correlated features, potentially underestimating their importance. When a feature is shuffled, the model might rely on a correlated feature with similar information, reducing the observed importance of all correlated features. To address this, we performed PI analysis on the GA-selected feature sets of the four RF models in two ways: 1) individually for each feature, ignoring correlations, and 2) by considering each feature correlation group. The latter analysis involves first performing hierarchical clustering (Nielsen, 2016) of the GA-selected feature set into correlation groups. This was done such that the average absolute Spearman's pairwise correlation between each group is less than 0.7. In other words, we use average linkage with absolute Spearman's correlation as a measure of distance in the feature clustering. Next, we study each feature group individually by shuffling the values of all features in the corresponding group. In this way, the results of the PI analysis are more robust against feature correlation and better highlight the core information sources and their relative significances in peat thickness modeling. The feature group importance is measured in terms of mean overall accuracy decrease (MAD) which indicates how much the prediction performance of the model decreases on average if the corresponding feature group values are shuffled, i.e., permuted.

2.4.0.3.3. Shapley additive explanations. Shapley additive explanations (Štrumbelj and Kononenko, 2014; Padarian et al., 2020), or SHAP values, are a way to explain the contribution of each feature to the output of a ML model. SHAP values use a game theoretic approach to measure a player's contribution to the outcome of a player coalition. In our context, a player refers to a feature of interest and the coalition to a group of other features. In this work, we apply the Saabas approximation, which is used in tree-based models for calculating the feature SHAP values (Loecher et al., 2022). The SHAP values presented in this study can be interpreted as the log odds of the corresponding peatland thickness class prediction, i.e., with a higher SHAP value, the probability of a peatland class increases and vice versa.

2.4.0.4. Performance evaluation and metrics

2.4.0.4.1. Model training and testing performance. A 70 % subset of the reference dataset was reserved for model training. As discussed in section 2.2.4, the validation sets are naturally part of the reference training set due to cross-validation approach used. In this work, we used 3-fold stratified cross-validation (CV) for estimating the performance of the RF models in the training phase. Stratified CV is a technique used in ML to ensure that each fold of the CV process preserves the same data distribution in the training and validation sets as the original dataset (Hastie et al. 2001). This is particularly useful when dealing with imbalanced datasets. If data imbalance is not considered in the CV process, the model might be validated with a set of data observations completely lacking in the training set. By taking the data distribution into account in the folds, the model performance is validated with data corresponding to the data distributions it was trained with. In terms of

model training and feature selection using GA, we employed the stratified CV to assess model performance at each optimization stage. After the post-training and feature selection, the trained models underwent testing using the reference data isolated to an independent out-of-sample test set. It contains 30 % of all reference data, equaling approximately one million data observations.

2.4.0.4.2. Performance metrics and map presentations. The model performances in training and testing phases were evaluated using five key metrics: overall accuracy, F1-score, (Goutte and Gaussier, 2005), producer's accuracy, user's accuracy, and balanced overall accuracy. Overall accuracy is a common evaluation metric used in classification tasks to measure the percentage of correctly predicted instances out of the total instances in the dataset. F1-score is the harmonic mean of precision and recall, providing a balanced measure of a model's accuracy. Overall accuracy can be influenced by imbalanced data, with an unequal number of positive and negative cases. In such cases, balanced accuracy is preferred. It is calculated as the mean of sensitivity and specificity. F1 score is still useful with imbalanced data but it focuses on the performance of the positive cases. 95 % confidence intervals were also estimated for overall accuracy and balanced accuracy based on binomial test and for F1-score using bootstrapping method to facilitate evaluation and comparison between models and data sets.

Producer's accuracy is a metric used to measure the class-wise proportion of true predictions out of all actual corresponding class instances in the data set. It represents the ability of a model to predict a specific class of interest and is calculated as the number of correctly predicted class instances divided by the total sum of the class instances in the data set. Similarly, user's accuracy is a metric for measuring the class-wise proportion of all correctly made class predictions from all the class predictions the model has made. In other words, user's accuracy indicates how frequently the model predicts a particular class correctly and is calculated class-wise as the number of correct class predictions divided by the number of all class made predictions.

Furthermore, a receiver operating characteristic (ROC, Fawcett, 2006) analysis was conducted for the CV results. The ROC curve and its corresponding area under the curve (AUC) give a comprehensive measure of a binary classifier's performance with all possible classification probability decision thresholds. The AUC value can be interpreted as the probability that a classifier is able to correctly rank a randomly selected negative (0) and a positive (1) observation.

Final discretized map presentations were derived from the predicted probability maps utilizing the ROC analysis. The threshold values used for the discretization of the probabilities were computationally determined as the thresholds in the corresponding ROC-curves. The optimal threshold with corresponding point on the ROC curve minimizes the distance from the point on the ROC-curve to the top-left corner, i.e., the point where TPR = 1 and FPR = 0. In other words, the computational threshold aims to simultaneously maximize correct predictions and minimize false predictions (TPR and FPR values, respectively).

2.4.0.5. Comparison to legacy maps

The RF predictions were compared against peat and non-peat areas of legacy soil maps to evaluate the potential improvements of the predictions in the mapping of peatlands. The comparison was made in terms of accuracy at point locations of the reference data, spatial distribution of peatland areas, and total peatland area in Finland.

The comparisons were made against the Superficial deposit map with a scale of 1:20,000 (GTK, 2015) covering approximately 37 % of the land area of Finland, and the Superficial deposit map with scale of 1:200,000 covering the entire country. The comparison at point locations was done for the respective coverage areas of the maps and the comparison of spatial distribution of peatland areas at a sample area. The total peatland area comparison was made only against a 1:200,000 scale map.

The reference data for the comparison at point locations included the post-2009 observations from the out-of-sample test data (n = 377,000) to exclude observations that may have been used for making the superficial deposit maps. The comparisons were made between the $\geq$ 0.4 m thick peat areas in the 1:20,000 map and the RF40 prediction, and between the $\geq$ 30 cm and $>$ 60 cm thick peat areas in the 1:200,000 map and the RF30 and RF60 predictions, respectively. The comparison results against the 1:200,000 map are also applicable for the Finnish Soil Database (Lilja et al., 2017), which is a derivative of the 1:200,000 map but follows a different soil classification system. These two maps are yet the only spatially continuous maps of the peatlands in the country covering all land uses.

3. Results

3.1. Peatland classification performance

The stratified CV produced (train) and out-of-sample (test) performance metrics for the peatland thickness RF10, RF30, RF40 and RF60 classification models are presented in Table 3. Also, the distributions of negative and positive samples are presented. Recall that each of the peatland thickness class cases (RF10, RF30, RF40, RF60) were treated as separate binary modeling cases as described in detail in Section 2.4.1.

Overall, the model performances show good results with all metrics. Overall accuracy and F1-score values ranged 86–96 % and 0.82–0.95, respectively. The 95 % confidence intervals for the test data metrics were narrow and non-overlapping. The CV estimates and out-of-sample results are very similar, with the out-of-sample results showing slightly better model performance. The overall classification performance decreases from RF10 model to RF60 model roughly 6–7% indicating that modelling of the lowest peat thicknesses (RF10) performs extremely well but the higher peat thickness models (RF30, RF40, RF60) contain lower prediction reliability. However, the data distributions show that the fraction of negative samples increases and positive decreases as peatland thickness threshold is increased (10, 30, 40, 60 cm). The influence of this moderate imbalance on overall accuracy was negligible (~0.2 %) based on testing with balanced accuracy metrics.

The user's and producer's accuracies range from 77—96 % and 85–96 % respectively. The lowest user's accuracy values are for the RF60 positive (1) classification. In other words, with higher peat thickness RF models are more likely to make false positive predictions than the lower thickness models. The RF model consistently demonstrates high producer's accuracies, which indicates that it is very effective at accurately identifying areas with actual corresponding peat thickness.

The ROC curves presented in Fig. 3 and their AUC values ranging between 0.90–0.99 well agree with the other performance metric results. The AUC values are higher for the low thickness RF models than for the thicker peat models. All four models achieve greater than 90 % true positive rates (TPR) along with false positive rates (FPR) of 15 %.

3.2. Feature selection

Feature selection and analysis results are presented in Fig. 4, Table 4 and Table 5. The full list of features can be found in T able A3 in A ppendix A. Fig. 4 represents the rankings of the top five feature groups in descending order of importance in terms of the MAD value. Standard deviations of the respective MAD values were also calculated but are not visualized in Fig. 4 due to the deviation values being indistinguishably small, which indicates the results are highly stable.

In total, 26, 33, 27, and 29 features were selected by GA for the RF10, RF30, RF40 and RF60 models, respectively. In models RF10, RF30, and RF40, the first feature group has a significantly higher importance compared to other groups. The peatland thickness classification performance decreases approximately 34 %, 14 %, 25 %, and 10 % for RF10, RF30, RF40 and RF60, respectively, when the top feature group values are shuffled in the presence of other feature groups. In RF10,

Table 3
Cross-validation (train) and out-of-sample (test) results for all RF-models in terms of overall accuracy, F1-score values and class-wise user's and producer's accuracies. Distributions of the negative (0; does not belong to the thickness class) and positive (1; belongs to the thickness class) samples are also presented. The train 0, train 1, test 0, test 1 labels refer to class-wise (0/1) cross-validated (train) and out-of-sampled (test) estimated user's and producer's accuracy values. 95 % confidence intervals for overall accuracy and F1-score are given in brackets.

	Overall accuracy %		F1-score		Negative (0) samples %		Positive (1) samples %	
Model	**train**	**test**	**train**	**test**	**train**	**test**	**train**	**test**
RF10	94.70	95.60 (95.57–95.65)	0.95	0.95 (0.954–0.954)	52.09	52.25	47.91	47.75
RF30	93.40	94.30 (94.26–94.35)	0.93	0.94 (0.937–0.938)	54.88	55.05	45.12	44.95
RF40	91.70	92.90 (92.88–92.98)	0.91	0.92 (0.919–0.920)	57.20	57.34	42.80	42.66
RF60	85.90	89.10 (89.03–89.15)	0.82	0.85 (0.854–0.856)	63.58	63.56	36.42	36.44
	User's accuracy %				Producer's accuracy %			
Model	**train 0**	**test 0**	**train 1**	**test 1**	**train 0**	**test 0**	**train 1**	**test 1**
RF10	95.60	95.60	93.80	95.60	94.20	96.00	95.30	95.20
RF30	95.50	95.80	91.00	92.60	92.30	93.80	94.70	94.90
RF40	95.00	95.50	87.80	89.70	90.30	92.00	93.60	94.20
RF60	91.90	93.00	77.30	82.90	85.40	89.60	86.80	88.20

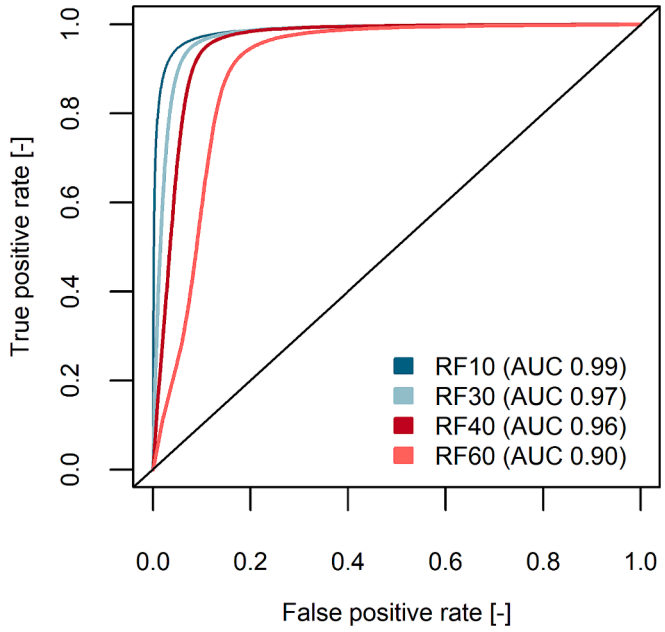

Fig. 3. Receiver Operating Characteristic (ROC) curves for all four RF models and corresponding Area Under the Curve (AUC) values.

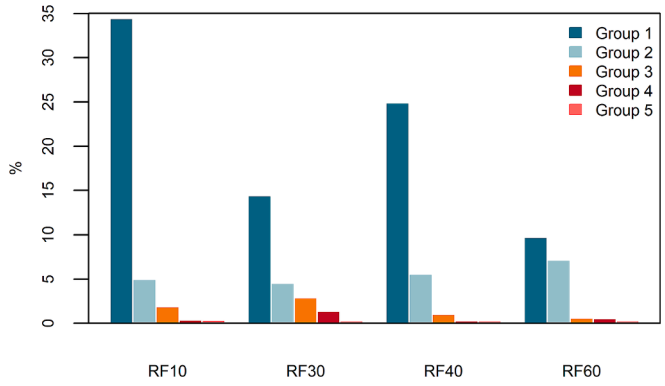

Fig. 4. Mean accuracy decrease (MAD) values of top five feature groups of the RF-models. The feature groups and their individual features are listed in Table 5.

RF30 and RF40 cases, the DTW 2 ha, DEM CVA 5x5 mean, DEM var 31x31 mean, and DEM var 31x31 std features contribute the most to the prediction performance, while AR K and AR Th have the highest importance for the model RF60. The abovementioned features are, however, present in the top two feature groups of all the RF models. It can also be seen that with increasing peatland thickness, the NDSI, kNDVI and NBR features increase their importance, while their importance is smaller when compared with AR, DTW and geomorphometric features. In contrast to the other models, the geomorphometric and AR feature groups are more important for the RF60 model than the lower thickness models. In these lower peat thickness models, feature groups containing geomorphometric features hold more significance over the AR feature groups.

The SHAP values calculated for 10 features in the top five groups (presented in Table 5) are shown in Fig. 5 as layered violin plots. The figure illustrates the relationship between the values of the most important GA-selected features and the corresponding SHAP value. The SHAP values indicate that small values of DTW 2 ha, DEM var 31x31 mean, DEM var 31x31 std, AR K, and AR Th contribute positively to the occurrence of peatlands, and large values of DEM CVA 5x5 mean and DEM CVA 11x11 mean contribute negatively to the occurrence of peatlands. Amongst the selected features, the DEM var 31x31 mean is consistently found to contribute to all peatland thickness models. The AR Th contributes to the RF60 model, exhibiting a similar inversely proportional relationship with the SHAP value. Additionally, kNDVI, NDVI, NBR, and NDSI contribute to the SHAP values in varying degrees, although their impact is relatively small. Overall, the SHAP analysis results agree with the PI analysis in Fig. 4 and Table 5.

3.3. Peatland predictions

The predicted probabilities and corresponding binary classifications for peatland thickness models are presented in Fig. 6 and Fig. 7, respectively. The binary classification rasters in Fig. 7 were classified from probability rasters in Fig. 6 using the ROC-curve based probability threshold values (see 2.4.4.2) of 0.534, 0.531, 0.5, and 0.42 for RF10, RF30, RF40, and RF60, respectively. According to these values, a smaller prediction probability is required for positive classifications in thicker peatland predictions (RF60) than in the shallower peatland predictions (RF10, RF30, RF40).

In Fig. 8, we present the corresponding agreement rasters for the model classifications as a sample from Oulujoki River. As discussed in Section 2.4.2.2, the agreement value (interval 50–100) measures the maximum number of decision trees that agree on the corresponding classification. For the Oulujoki River area, the average agreement for RF10, RF30, RF40, and RF60 is similar (79–81), but the spatial distribution of agreement differs. Inside of the RF10, RF30, RF40, and RF60 classified peat areas (as in Fig. 7), the mean agreement is the highest for RF10 (85) and the lowest for RF60 (67), whereas outside of the classified peat areas the mean agreement is the highest for RF60 (84) and the lowest for RF10 (78).

Furthermore, as also discussed in Section 2.4.2.2, we examined the

Table 4
List of GA selected features for RF-models and their permutation importance scores in terms of mean accuracy decrease (MAD %) without considering feature correlation. Feature are listed in decreasing order of MAD.

RF10		**RF30**	
AR K	4.98	AR K	4.55
DTW 2 ha	2.93	DTW 2 ha	1.94
DEM CVA 5x5 mean	2.87	DEM CVA 5x5 mean	1.87
DEM var 31x31 mean	1.77	DEM var 31x31 mean	1.26
DEM slope var 31x31 mean	0.52	DEM slope var 31x31 mean	0.33
DEM SAR 3x3 std	0.49	DEM SAR 3x3 std	0.26
DEM CVA 31x31 mean	0.33	DEM var 31x31 std	0.12
DEM var 31x31 std	0.22	AEM Im	0.1
DEM CVA 5x5 std	0.16	NDSI 1.6.-30.6.2021	0.1
NDSI 1.6.-30.6.2021	0.15	NDSI 15.6.-15.7.2021	0.09
SAVI 15.6.-15.7.2021	0.14	DEM CVA 31x31 mean	0.09
NDSI 15.6.-15.7.2021	0.13	SAVI 1.7.-31.7.2021	0.08
NDVI 15.6.-15.7.2021	0.11	Shoreline	0.07
NBR 1.4.-30.4.2021	0.1	SAVI 15.6.-15.7.2021	0.07
Shoreline	0.08	NBR 1.4.-30.4.2021	0.07
SAVI 15.7.-15.8.2021	0.08	TCTw 15.4.-15.5.2021	0.06
EVI2 15.5.-15.6.2021	0.08	kNDVI 1.6.-30.6.2021	0.06
NDVI 1.5.-31.5.2021	0.08	NDVI 1.5.-31.5.2021	0.06
SAR Ratio 21.5.-10.7.2021	0.05	NBR 1.6.-30.6.2021	0.06
SAR VV 1.9.-30.11.2021	0.05	DEM SAR 3x3 mean	0.05
SAR VV 1.4.-20.5.2021	0.04	NDSI 15.9.-15.10.2021	0.04
SAVI 1.4.-30.4.2021	0.03	SAR VV 11.7.-31.8.2021	0.04
NDSI 15.8.-15.9.2021	0.03	SM 15.6.-15.7.2021	0.04
SAR Ratio 1.4.-20.5.2021	0.02	DEM CVA 31x31 std	0.04
TCTb 1.9.-31.9.2021	0.02	TCTw 1.5.-31.5.2021	0.03
AR K/Th	0	NDVI 1.9.-31.9.2021	0.03
		DEM CVA 11x11 mean	0.03
		TCTw 15.8.-15.9.2021	0.02
		SAR VV 1.4.-20.5.2021	0.02
		SAVI 1.5.-31.5.2021	0.01
		NDSI 1.10.-31.10.2021	0.01
		EVI2 15.4.-15.5.2021	0.01
		EVI2 1.10.-31.10.2021	0
RF40		**RF60**	
AR K	5.56	DEM var 31x31 mean	4.83
DEM CVA 5x5 mean	2.27	AR K	4.38
DTW 2 ha	1.73	AR Th	3.5
DEM var 31x31 mean	1.64	DEM CVA 11x11 mean	0.57
DEM slope var 31x31 mean	0.89	DEM var 31x31 std	0.37
NDVI 1.5.-31.5.2021	0.18	SAVI 1.4.-30.4.2021	0.26
NBR 1.6.-30.6.2021	0.1	DEM slope var 31x31 std	0.22
DEM CVA 31x31 std	0.1	kNDVI 1.6.-30.6.2021	0.18
SAVI 15.6.-15.7.2021	0.08	TCTw 1.4.-30.4.2021	0.15
NBR 15.4.-15.5.2021	0.08	TCTw 15.4.-15.5.2021	0.14
SAVI 1.4.-30.4.2021	0.07	SAVI 15.6.-15.7.2021	0.14
TCTw 1.4.-30.4.2021	0.06	NDSI 1.7.-31.7.2021	0.13
TCTw 1.5.-31.5.2021	0.05	EVI2 1.5.-31.5.2021	0.11
NDSI 1.6.-30.6.2021	0.05	NDSI 15.7.-15.8.2021	0.11
NDSI 15.6.-15.7.2021	0.05	NBR 1.6.-30.6.2021	0.09
Shoreline	0.05	TCTb 15.6.-15.7.2021	0.09
DEM slope var 31x31 std	0.05	TCTw 1.5.-31.5.2021	0.09
kNDVI 1.6.-30.6.2021	0.04	TCTw 1.7.-31.7.2021	0.07
SAR VV 21.5.-10.7.2021	0.04	kNDVI 15.7.-15.8.2021	0.07
NDSI 15.9.-15.10.2021	0.04	NDSI 15.6.-15.7.2021	0.07
TCTw 1.9.-31.9.2021	0.04	NDSI 15.4.-15.5.2021	0.07
NDSI 1.7.-31.7.2021	0.03	TCTb 1.6.-30.6.2021	0.06
kNDVI 15.7.-15.8.2021	0.03	NDSI 15.8.-15.9.2021	0.05
SAVI 15.5.-15.6.2021	0.02	SAR Ratio 11.7.-31.8.2021	0.04
SAR VV 11.7.-31.8.2021	0.02	TCTg 15.6.-15.7.2021	0.03
TCTg 1.9.-31.9.2021	0	NDVI 1.8.-31.8.2021	0.02
SM 15.6.-15.7.2021	−0.01	TCTb 1.9.-31.9.2021	0
		SM 15.8.-15.9.2021	−0.07
		SM 15.6.-15.7.2021	−0.08

relationship between agreement values of RF models and corresponding classification performance. Fig. 9 shows that they have a very strong non-linear relationship, and the fitted second-order polynomial function describes their relationship with high accuracy. The polynomial function fit score R^2 is over 0.99 for all RF model cases. The polynomial functions allow the conversion of agreement maps into accuracy maps, which are shown for the Oulujoki River in Fig. A4 in the A ppendix A.

Table 5
Top five feature groups for RF-models. See Table 2 for explanation of the feature names.

Group	RF10	RF30	RF40	RF60
1	DTW 2 ha, DEM CVA 5x5 mean DEM var 31x31 mean DEM var 31x31 std	DTW 2 ha DEM var 31x31 mean DEM var 31x31 std	DTW 2 ha DEM CVA 5x5 mean DEM var 31x31 mean	AR K AR Th
2	AR K	AR K	AR K	DEM var 31x31 mean DEM var 31x31 std
3	DEM slope var 31x31 mean DEM SAR 3x3 std	DEM CVA 11x11 mean DEM CVA 5x5 mean	DEM slope var 31x31 mean DEM slope var 31x31 std	kNDVI 1.6.-30.6.2021 kNDVI 15.7.-15.8.2021 NDVI 1.8.-31.8.2021 NBR 1.6.-30.6.2021
4	NDSI 1.6.-30.6.2021 NDSI 15.6.-15.7.2021	DEM slope var 31x31 mean DEM SAR 3x3 mean DEM SAR 3x3 std	NDSI 1.6.-30.6.2021 NDSI 1.7.-31.7.2021 NDSI 15.6.-15.7.2021	DEM CVA 11x11 mean
5	DEM CVA 31x31 mean	NDSI 1.6.-30.6.2021 NDSI 15.6.-15.7.2021	kNDVI 1.6.-30.6.2021 kNDVI 15.7.-15.8.2021 NBR 1.6.-30.6.2021	NDSI 1.7.-31.7.2021 NDSI 15.6.-15.7.2021

Visual inspection of the accuracy maps in the a ppendix reveals that the areas with the highest number of peatland predictions, specifically the central, northeast, and southeast regions, show average classification accuracies ranging from 82—85 %.

The predicted occurrence of peatlands in the whole of Finland is shown in Fig. 10. Peatland occurrence is the highest in western and northern Finland. The total predicted areas of $\geq$ 10 cm, $\geq$ 30 cm, $\geq$ 40 cm, and $>$ 60 cm are 86,669 km^2, 75,991 km^2, 73,364 km^2, and 60,118 km^2, respectively. They represent 29 %, 25 %, 24 %, and 20 % of the total land area of the country (303,948 km^2), respectively.

3.4. Comparison to legacy maps

The comparison against point locations of the reference data indicates that RF predictions have similar accuracy than the 1:20,000 map and higher accuracy than the 1:200,000 map, as shown in Table 6. The main improvement of RF predictions to the 1:200,000 map is that they correctly identify a higher number of peat occurrences ($\geq$ 30 cm, $>$ 60 cm), particularly in the case of the thickest peat ($>$ 60 cm). The used test data was imbalanced (12–25 % peat observations), and thus, the 'balanced overall accuracy' in Table 6 may be a better metric than the 'overall accuracy'. The narrow and non-overlapping confidence intervals for overall accuracy and F1-score further indicate that the performance of different models and data are statistically different.

The comparison of spatial distribution of peatland areas at the sample area in Fig. 11 shows that predicted peatland areas broadly identify the same peatland areas as the 1:20,000 and 1:200 000 maps, but there are differences in peatland extents, delineation of peatlands from non-peatlands, and number of identified peatland areas. The RF predictions suggest often larger peatland areas, they provide a spatially more refined description of peatland boundaries, and they predict more individual peatland areas than the 1:20,000 and 1:200 000 maps. These differences are a result of different production methodologies and the spatial detail of the maps. The RF predictions are based on ML and a range of spatially consistent data, whereas the superficial deposit maps

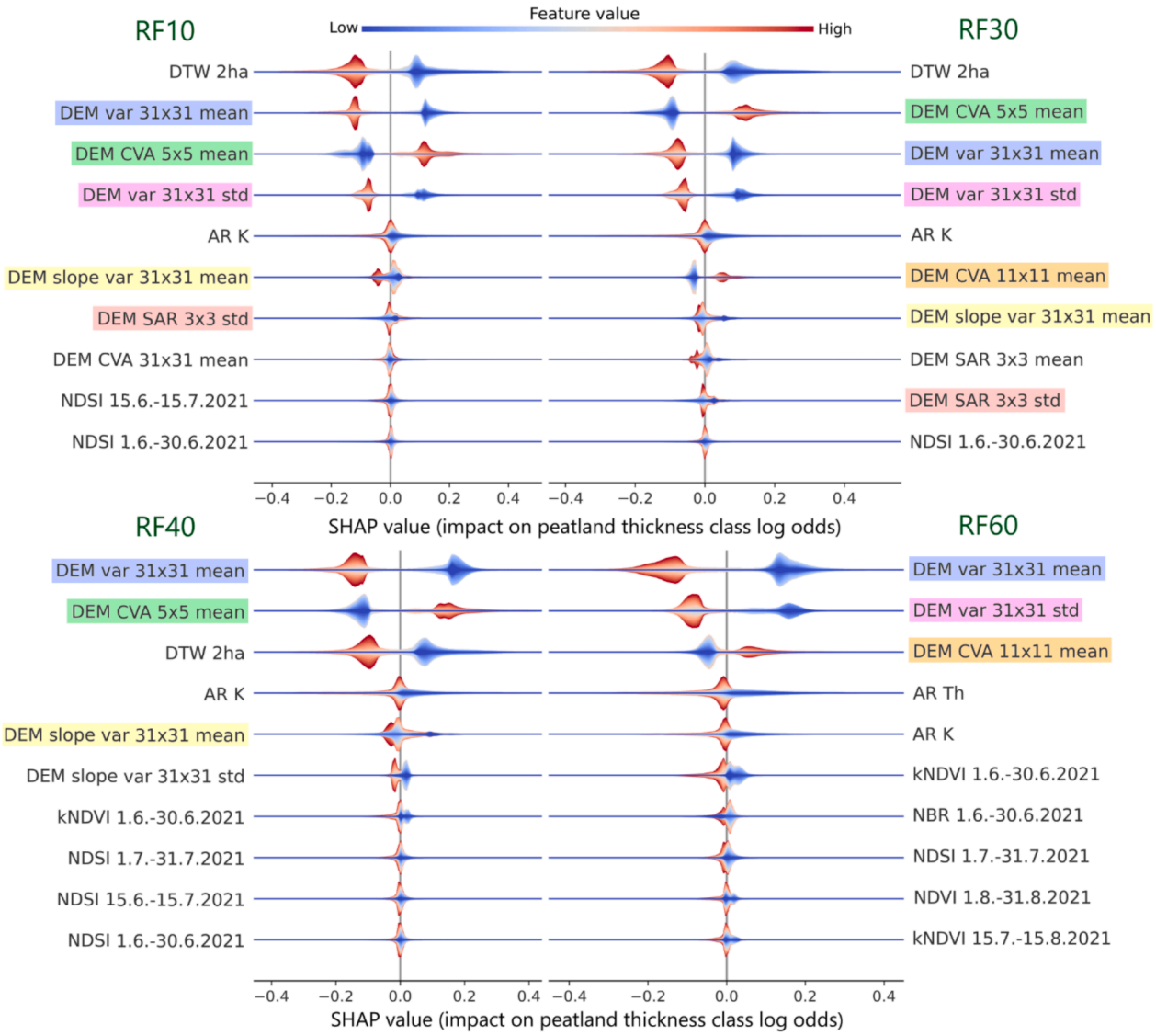

Fig. 5. The SHAP values for the peat thickness classification models RF10, RF30, RF40, and RF60. Only 10 features in the top five feature groups (Table 5) are included for visualization purposes. SHAP value indicates the impact of a feature on the model output. High SHAP values correspond to an increasing impact on the probability of a positive classification, while low SHAP values correspond to a decreasing impact. Feature value coloring shows how low and high feature values correlate with the SHAP value. The wide sections of the violin represent areas of high density of observed feature values in the data. Repeating DEM features over the RF models are colored to ease the readability.

are based on field work (1:20,000/1:200,000) and human interpretation of aerial photographs (1:20,000) and geophysical data (1:200,000) (Haavisto, 1983; Yli-Halla et al., 2003). The RF predictions also have a grid cell size of 0.25 ha (50 m × 50 m), whereas the minimum mapping unit in the 1:20,000 map is 2–4 ha and in the 1:200,000 map 6.25 ha.

In terms of total peatland area in Finland, the RF predictions suggest a larger area than the Superficial deposit 1:200,000 map (GTK, 2010). The predicted total area of ≥ 30 cm (RF30) thick peat is 75,991 km^2, which is 14 % larger than in the 1:200,000 map. For ≥ 60 cm thick peat, the predicted total area is 60,118 km^2, which is 21 % larger than in the 1:200,000 map. The RF10 prediction suggests a total peatland area of 86,669 km^2, which is 29 % of the land area of the country (303,948 km^2). The differences result from the data production methods, as explained in the previous paragraph.

4. Discussion

4.1. Modelling approach

This research presents a comprehensive data processing and ML approach rarely demonstrated in DSM. By integrating airborne geophysical surveys, LiDAR-derived DEMs, optical and SAR satellite data, and geomorphological datasets, and organizing features to reduce correlation, we successfully applied ML trained on extensive, balanced ground reference data for national-scale mapping of peat thickness and extent (>300,000 km^2). For feature evaluation, we employed a novel SHAP analysis to assess the role and importance of spatial features. The results of the SHAP analysis were largely consistent with those from the PI method, indicating that the fluctuations in the values of the top-ranked features had the most significant effect on the outputs of the corresponding RF models. Additionally, we used the agreement of individual RF decision trees to assess prediction reliability—an often-overlooked method in DSM (Wadoux et al., 2020; Minasny et al., 2019). This agreement strongly correlated with overall accuracy,

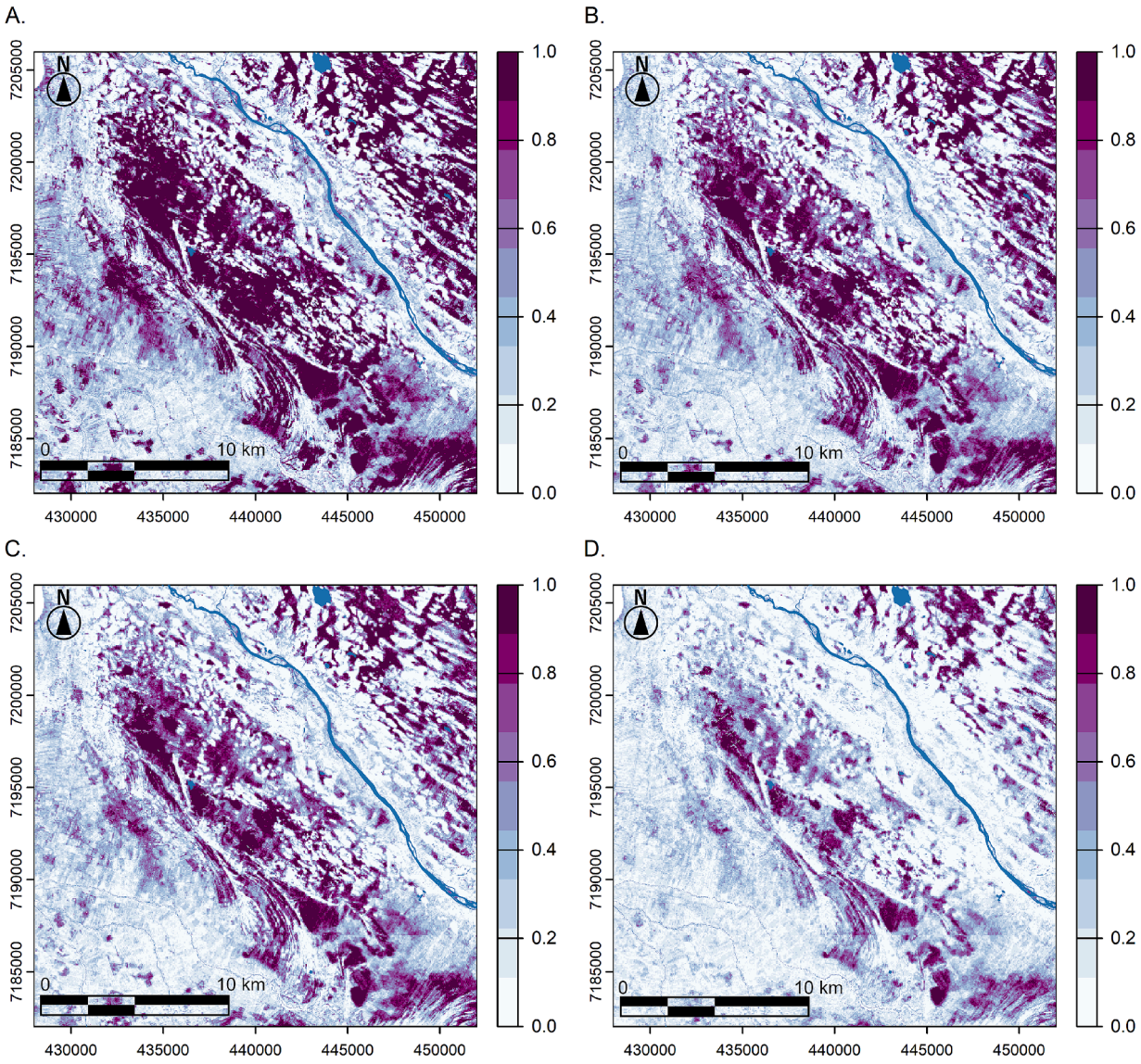

Fig. 6. Predicted probability for the occurrence of A. ≥ 10 cm, B. ≥ 30 cm, C. ≥ 40 cm, and D. > 60 cm thick peatland at Oulujoki River (WGS84: 64.9 N, 25.7 E). Map values 0–1 = 0–100 % probability. The figure axis units are in meters (m, coordinate system: EUREF-FIN).

enhancing the reliability of prediction maps and informing local uncertainty interpretation, especially where minimizing false positives or negatives is critical. Consequently, the predicted peatland boundaries, particularly for deposits > 60 cm thick, were more accurate than those in existing legacy maps.

Our predictions demonstrated high accuracy, achieving an overall rate of 96 % for peat layers ≥ 10 cm. Accuracy slightly declined for thicker layers, likely due to the models' increased difficulty in establishing decision boundaries based on feature data limitations related to peat thickness and the effects of less balanced data distributions (Kaur et al., 2019). Compared to recent studies on peat thickness and extent, our accuracies were similar or higher. In Sweden, accuracies of 88–92 % were reported in two studies (Ågren et al., 2022; Rimondini et al., 2023) using DEM-derived wetness and topographical indices to model peat depths of ≥ 30 cm, ≥40 cm, ≥50 cm, and ≥ 100 cm. In Scotland, Aitkenhead (2017) used neural networks with diverse covariates, Poggio et al. (2019) applied ML methods with satellite data, and O'Leary et al. (2022) relied on neural networks and radiometric data, achieving accuracies between 65 % and 96 %. In Finland, Lahti and Häme (1992) distinguished peatlands from mineral soils with 77 % accuracy before the advent of high-resolution data, while Antropov et al. (2014) applied L-band multitemporal polarimetric decompositions, achieving 55–70 % accuracy. These studies demonstrate that predicting peat occurrence at shallow depths (<1 m) can be successful; however, none matched the extensiveness of our study in terms of area, covariate application, and training data.

Among the predictors used for modeling peat thickness, DEM-derived features (DTW and geomorphometric indices) and airborne radiometric data were generally the most important. DTW predicts soil moisture gradients based on elevation changes along the least-slope path to the nearest surface water, identifying areas with high soil saturation that foster peat accumulation. However, DTW's importance decreases with thicker peat layers, suggesting it is better suited for predicting peat occurrence than thickness. The inclusion of geomorphometric features indicates that peatland microtopography differs from other soil types. Peatlands typically exhibit flat, smooth surfaces due to gradual accumulation, reflected in low DEM variation, slope variation, and surface area ratio. This flatness extends over broad areas, indicated by the large window sizes selected for DEM and slope variation. High circular variance of aspect (DEM CVA) further highlights the horizontality of Finnish peatlands, where minor topographical changes result in gradual slopes and highly variable aspects between DEM pixels. These findings align

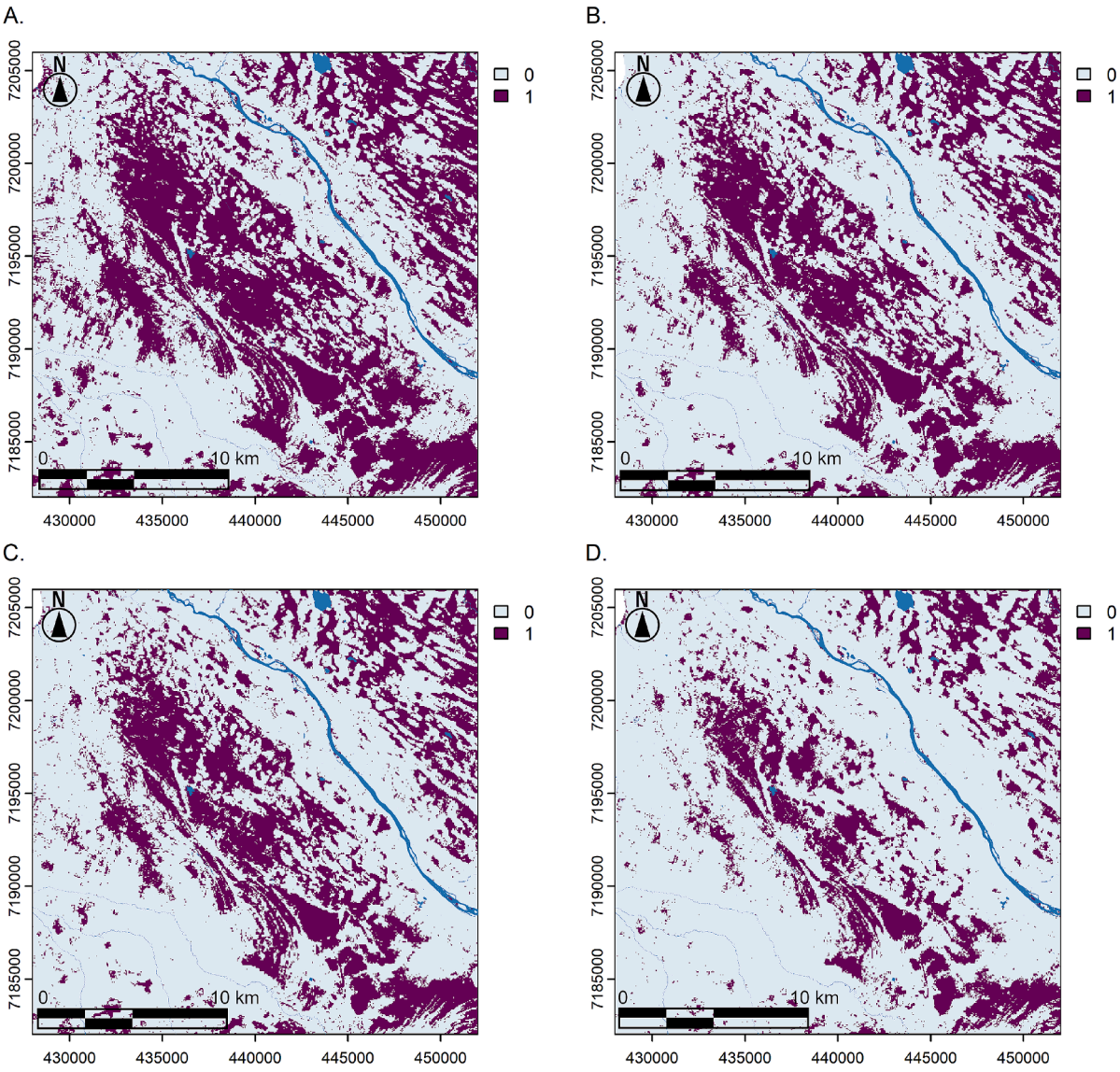

Fig. 7. Predicted occurrence of A. ≥ 10 cm, B. ≥ 30 cm, C. ≥ 40 cm, and D. > 60 cm thick peatland at Oulujoki River (WGS84: 64.9 N, 25.7 E). Map value 1 = belongs to thickness class, and 0 = does not belong to thickness class. The figure axis units are in meters (m, coordinate system: EUREF-FIN).

with Ågren et al. (2022) and Rimondini et al. (2023), who also used topographical indices to predict peat extent and thickness. However, regarding peat depth, such indices likely provide only indirect information, for example by distinguishing central peatland areas from edges.

Potassium radiation emerged as one of the most important radiometric predictors, with its significance, along with thorium radiation, particularly high in the RF60 model. These findings align with the established understanding that natural gamma radiation attenuates with increased soil water content (Reinhardt & Herrmann, 2019; Minasny et al., 2019). Gamma radiation was the only feature set providing subsurface physical information related to peat thickness (Davisson, 1968; Endrestøl, 1980), likely explaining why its importance surpassed DEM-derived features in predicting the thickest peat deposits. In contrast, electromagnetic components were not among the most important predictors, likely due to the airborne electromagnetic data's insensitivity to the less conductive topmost soil layers (Suppala et al., 2005).

Various satellite-derived features were also selected for predictions. Among optical data, vegetation indices such as NDVI, SAVI, kNDVI, and EVI2, along with the snow index (NDSI), soil color index (SCI), and burnt area index (NBR), showed the highest importance. NDVI, previously applied in peatland mapping (e.g., Shimada et al., 2016; Poggio et al., 2019; Karlson & Bastviken, 2023), was the most influential vegetation index in our analyses, alongside kNDVI. This likely reflects vegetation differences between pristine (i.e., undrained), forestry-drained, and cultivated peatlands compared to mineral soils. The significance of NDSI was unexpected but may be due to differences in the ratio of visible and shortwave infrared bands between peat and non-peat soils (Krankina et al., 2008; Riggs et al., 1994). SCI importance increased with peat thickness, suggesting color variations between shallow and deep peat deposits, though vegetation cover may also influence this. A similar trend was observed with Tasseled-Cap Transformation Wetness (TCTw), reflecting the higher moisture content typical of peatlands. The inclusion of NBR likely relates to vegetation cover differences, given its similarity to NDVI in formulation (Key & Benson, 1999). Poggio et al. (2019) also used NBR and NDSI to model peatland occurrence in Scotland.

None of the included Sentinel-1 SAR variables were highly important for predicting peat thickness, despite being selected through feature selection. Although SAR data is known to respond to soil moisture (Minasny et al., 2019; Toca et al., 2022), the C-band data used in this study proved insufficient for detecting peat soils, likely due to its limited

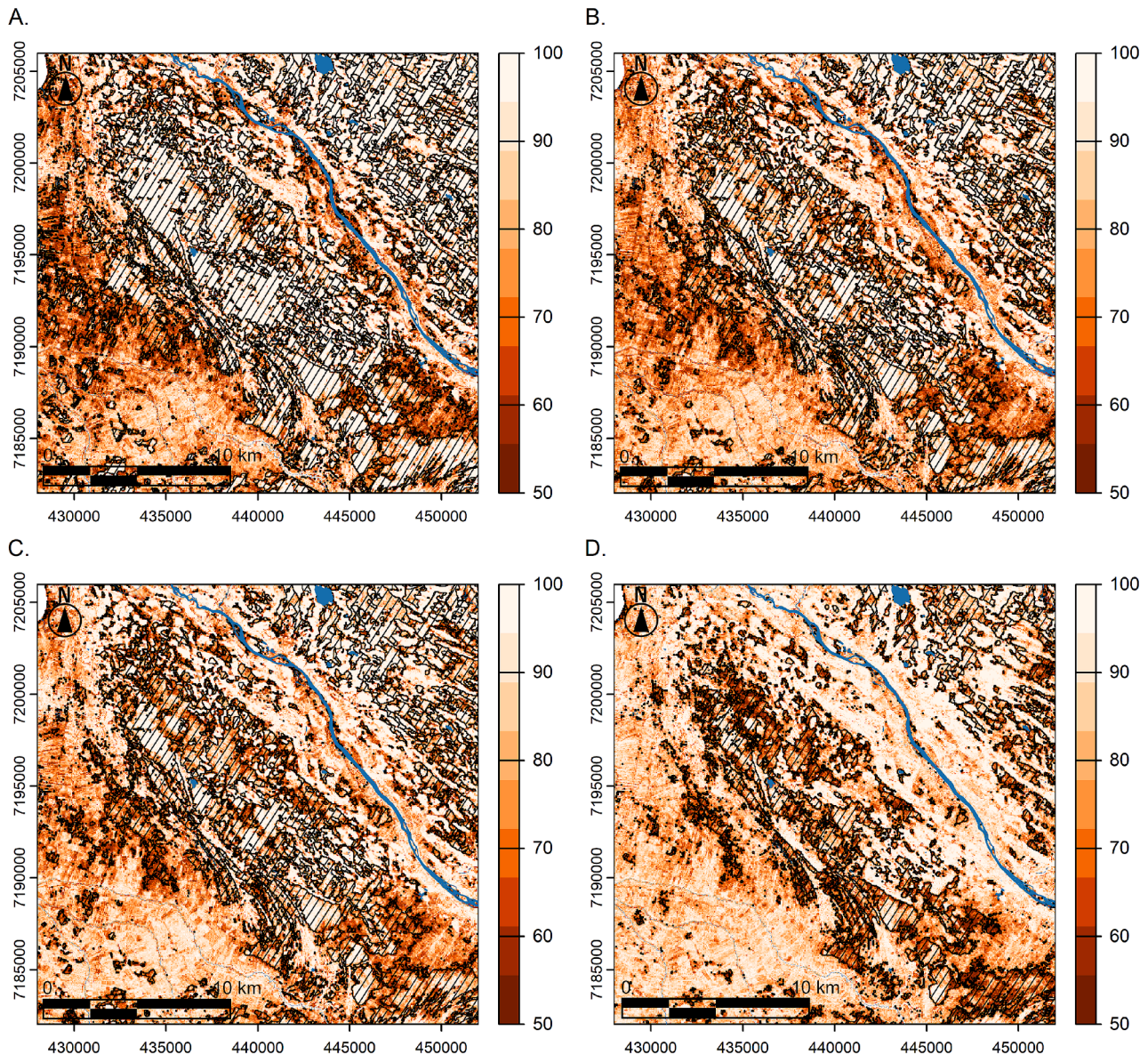

Fig. 8. Agreement of the RF decision trees on predicted class values (0 and 1) for A. RF10, B. RF30, C. RF40 and, D. RF 60 models at Oulujoki River (WGS84: 64.9 N, 25.7 E). Map value 50 = no agreement, and 100 = full agreement. Predicted occurrence of peat land areas with peat thickness of A. ≥ 10 cm, B. ≥ 30 cm, C. ≥ 40 cm, and D. > 60 cm (Fig. 7) are shown with hatched areas. The figure axis units are in meters (m, coordinate system: EUREF-FIN).

penetration through tree canopies. Additionally, the low importance may stem from SAR mosaic preprocessing, which averaged values over a long time-window, reducing the ability to detect local variations. l-band data, with better soil moisture detection capabilities, was not available for this study. Furthermore, GIS data on ancient shorelines did not prove relevant at the prediction scale used.

The resulting RF predictions for different peat depth classes, generated by independent models, can be integrated into a single data layer. However, this process requires some consideration, as independent models predicting various peat depth classes inevitably introduce contradictions. For example, RF60 predicted peat presence in certain pixels or small clusters where RF30 and RF40 did not. These discrepancies typically occurred in peatland edge or shoreline areas, where model uncertainties were higher, as indicated by lower regression tree agreement values. To resolve these inconsistencies, we propose tailored strategies based on the intended end-use of the data products. Contradictory areas can be classified as either peat or mineral soil by considering factors such as regression tree agreement values, consistency between models, and the types of errors (e.g., false positives or false negatives) most critical to end users.

The overall DSM methodology and feature selection approach applied in this study are broadly generalizable to other regions, as they rely on well-understood, non-location-specific methods. However, the specific features selected may vary depending on regional conditions. The features used here reflect the environmental characteristics of Finland and are likely generalizable to similar boreal regions. However, in areas with different climatic or topographical conditions, the relative importance of features may shift, necessitating further evaluation. For instance, the selection of geomorphometric indices employed in this study was tailored to Finland's topography, whereas gamma radiation has been consistently shown to be a highly predictive feature across diverse environments (Minasny et al., 2019).

4.2. *Limitations and future directions*

We conducted our analysis using a 50 m pixel size, primarily determined by the resolution of the available geophysical data, which limits the precision with which peatland extents can be delineated. Both the

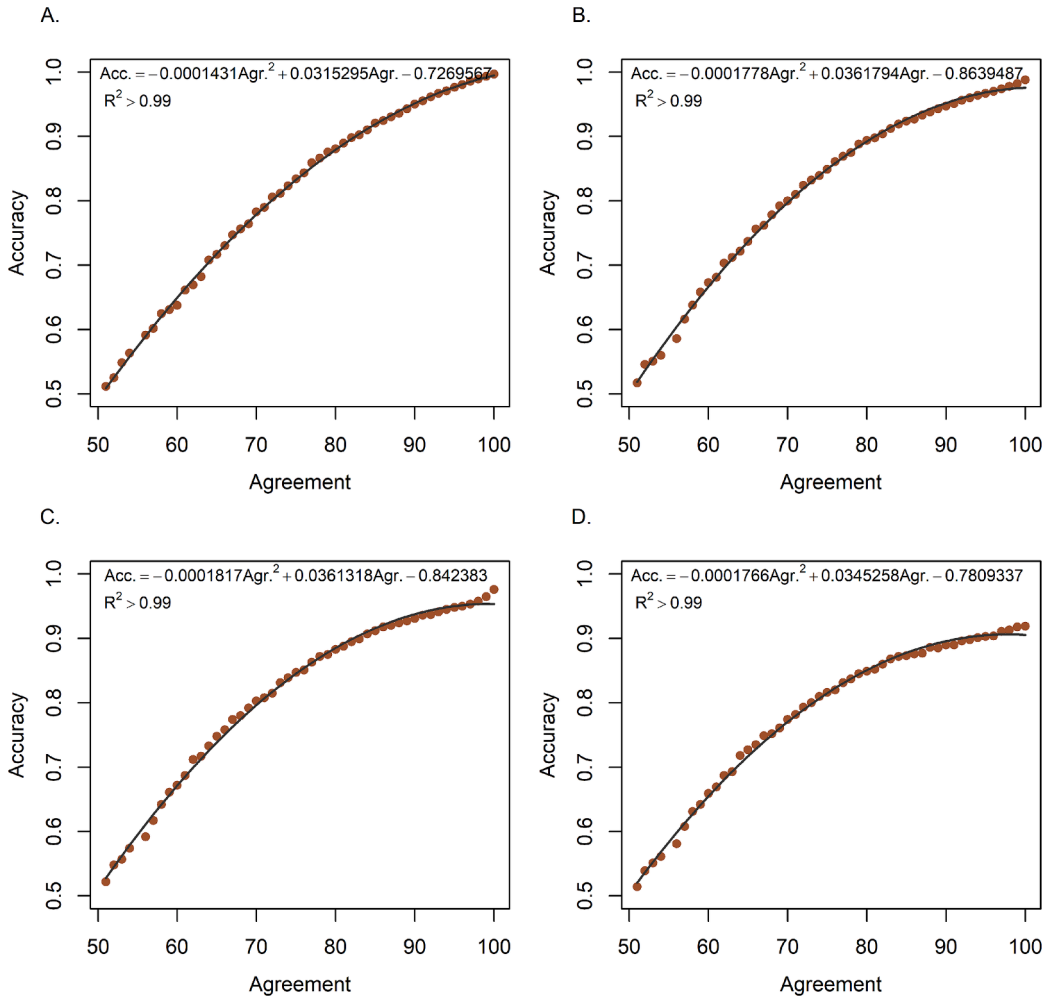

Fig. 9. Relationship between agreement of RF decision trees and overall accuracy for A. RF10, B. RF30, C. RF40 and, D. RF60 models. The lines are fitted polynomials of degree two; their equations and fit (R2) are also shown.

literature and our findings suggest that predictions could be generated at finer resolutions and for greater peat thicknesses (Rimondini et al., 2023; Lerssi et al., 2023). However, achieving this would likely require airborne geophysical data with denser flight tracks than those used in this study. Further exploration of opportunities to enhance both the spatial resolution and the range of peat thickness predictions is suggested.

Peat thickness was predicted using an exceptionally large set of soil observations. However, the data was imbalanced toward peat observations and required s upplementation with pseudo-mineral soil observations. This inevitably introduced some uncertainties, though they could not be quantified. Literature suggests that good predictive results can be achieved with less extensive soil observation data (e.g., Ågren et al., 2022; Rimondini et al., 2023), although most previous studies focused on smaller prediction areas. Peat observations were also often clustered together, as multiple soil samples were taken from each peatland patch. This clustering can result in spatial autocorrelation between observations, leading to model overfitting to local patterns and reducing generalizability to broader areas. While we addressed this issue, more detailed methods could have been employed than those used here. Additionally, in our soil observation data, the soil type (peat, non-peat) was often classified through sensory assessment, introducing another source of uncertainty. However, the classifications were carried out by highly experienced experts following established protocols. These aspects of the soil observation data underscore the importance of developing balanced, systematic, and cost-effective strategies for data collection, treatment, and utilization.

Peat thickness can vary over time, particularly in drained and managed peatlands (Mäkilä et al., 2013; Grønlund et al., 2008; Räsänen et al., 2023). This temporal variability affects both soil observations and feature data, as they may become inaccurate or outdated. In our study, changes in peat thickness were accounted for only in arable lands by adjusting soil observations, while potential effects on feature data—collected over different time periods—were not considered. Consequently, the updating and treatment of both soil observations and feature data, as well as the influence of peat thickness changes under different land uses, require further attention. Overall, the impact of various land uses on regional peatland predictions warrants additional investigation.

The wetness and vegetation conditions of peatlands typically vary seasonally, offering additional opportunities to differentiate peatlands from mineral soils, including variations in peat thickness. In the case of satellite data, the temporal dimension could be more effectively integrated into modeling. In our approach, satellite data from different months were treated as separate features; however, in reality, some datasets share the same time points, while others exhibit distinct temporal trajectories and trends. Notably, all satellite-derived features with higher permutation importance were from the summer months (June to August), when vegetation index values peak and moisture differences between peat and non-peat soils are most pronounced. Furthermore, incorporating meteorological data could enhance the information content of satellite imagery—for example, by identifying drought periods

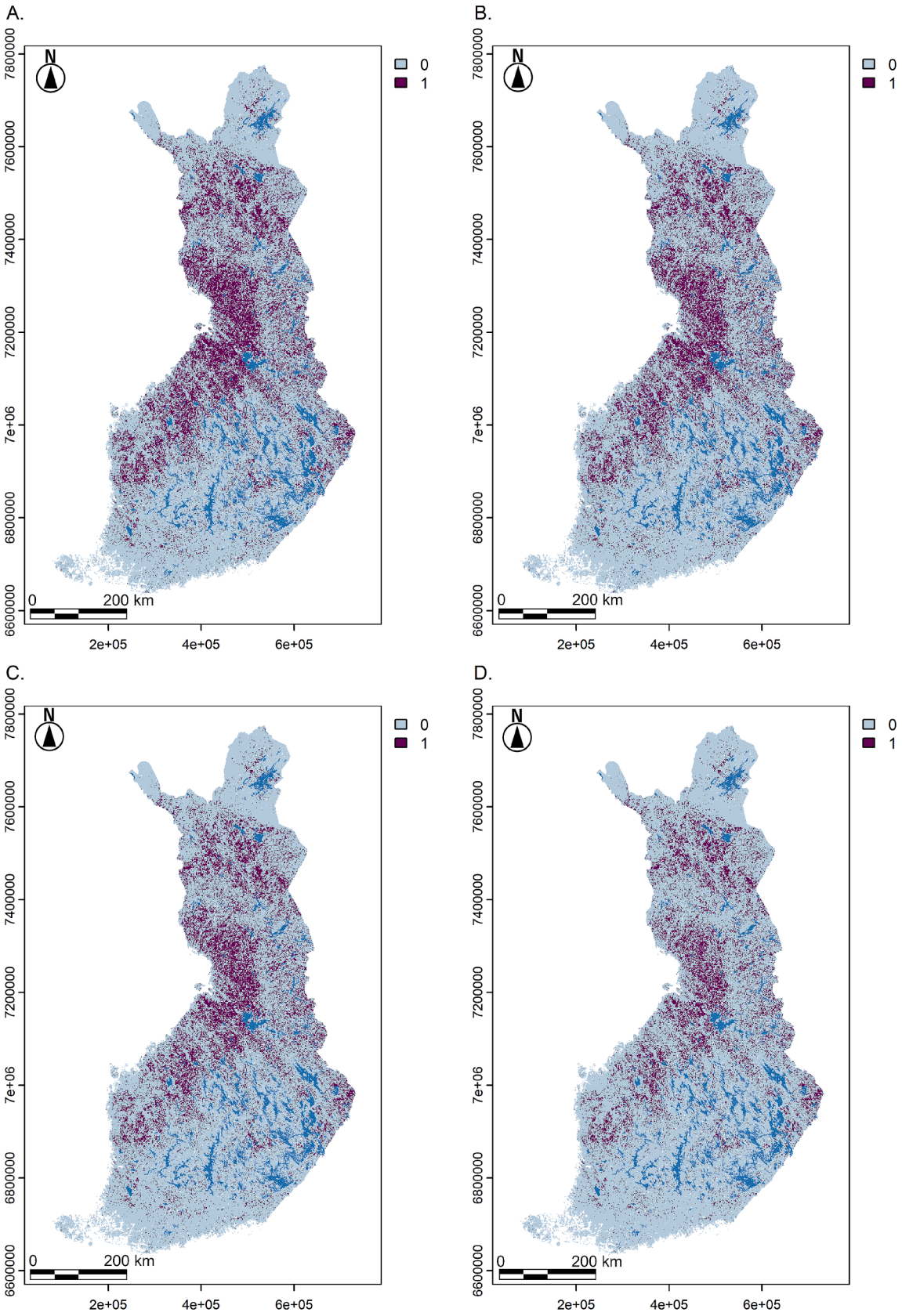

Fig. 10. Predicted occurrence of A. ≥ 10 cm, B. ≥ 30 cm, C. ≥ 40 cm, and D. > 60 cm thick peat in Finland. Map value 1 = belongs to thickness class, and 0 = does not belong to thickness class. The figure axis units are in meters (m, coordinate system: EUREF-FIN).

Table 6
Comparison of peatland occurrence between RF-model predictions and Superficial deposits (SD) 1:20,000 (37 % coverage of Finland; GTK, 2015 and 1:200,000 maps (full coverage of Finland; GTK, 2010). TPR = true positive rate, FPR = false positive rate. 95 % confidence intervals for accuracy and F1-score are given in brackets.

	Superficial deposits 1:20,000; Peat thickness ≥ 40 cm	RF40	Superficial deposits 1:200,000; Peat thickness ≥ 30 cm	RF30	Superficial deposits 1:200,000; Peat thickness ≥ 60 cm	RF60
Total observations	165,708	165,708	377,414	377,414	377,414	377,414
Peat observations	19,402	19,402	78,444	78,444	55,906	55,906
Overall accuracy (95 % CI)	0.967 (0.966–0.968)	0.959 (0.958–0.960)	0.929 (0.928–0.930)	0.944 (0.943–0.944)	0.912 (0.911–0.913)	0.923 (0.922–0.923)
Balanced overall accuracy (95 % CI)	0.932 (0.931–0.933)	0.921 (0.92–0.922)	0.889 (0.888–0.890)	0.927 (0.926–0.928)	0.820 (0.819–0.821)	0.889 (0.888–0.890)
F1-score (95 % CI)	0.861 (0.857–0.865)	0.833 (0.830–0.837)	0.830 (0.828–0.832)	0.871 (0.870–0.873)	0.720 (0.717–0.722)	0.782 (0.780–0.785)
TPR	0.897	0.872	0.821	0.898	0.681	0.838
FPR	0.032	0.030	0.042	0.044	0.042	0.061

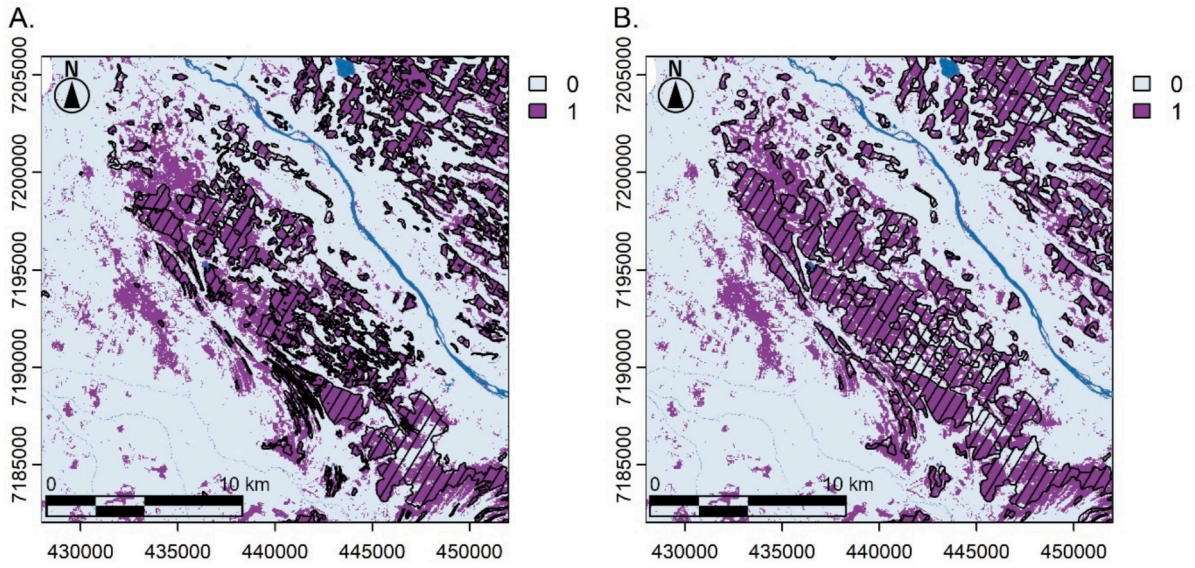

Fig. 11. Spatial comparison of A) RF40 peatland areas with peatland areas (≥ 40 cm) of Superficial deposits 1:20,000 (GTK, 2015), and B) RF30 peatland areas with peatland areas (≥ 30 cm) of Superficial deposits 1:200 000 (GTK, 2010) at Oulujoki River (WGS84: 64.9 N, 25.7 E). Map value 1 = belongs to thickness class, and 0 = does not belong to thickness class. Peatland areas of the Superficial deposits maps are shown as hatched areas. The figure axis units are in meters (m, coordinate system: EUREF-FIN) and y-axis is towards north.

that may cause vegetation stress on dried sites.

The regression tree agreement data provided valuable spatial insights into prediction uncertainties, highlighting areas where the models faced challenges in classification, particularly along peatland edges and shorelines. While we did not conduct an in-depth evaluation of spatial uncertainty, these observations suggest that further analysis of spatial factors influencing prediction accuracy could potentially enhance the DSM of peatlands.

Hyperparameter tuning is also a central aspect in ML, but we used a fixed number of 100 decision trees in the RF binary classification models for a suitable balance between predictive performance and computational efficiency, as suggested for example by Oshiro et al. (2012). The potential benefits of hyperparameter tuning in large scale digital mapping of peatlands is reserved for future work. Future studies should also investigate more advanced ML methods, such as convolutional neural networks (CNN; e.g., Pittman & Hu, 2022). These methods could be used to predict peat thickness as a continuous variable instead of class variable, and they could account for spatial correlation in peatland occurrence.

4.3. *Broader implications*

The results demonstrated that ML-based DSM can provide accurate and consistent data on peatlands in line with national and international soil classification systems (e.g., IUSS Working Group WRB, 2022; IPCC, 2019). This offers cost-effective opportunities to harmonize national peatland maps for the implementation of national and international policies, such as the EU Soil Strategy 2030 (European European Commission, 2021), EU Water Framework Directive (European Parliament and Council, 2000), and the Kyoto Protocol (UN, 1997), aimed at maintaining soil health and good status of surface waters, and reducing greenhouse gas emissions. For example, data produced through this approach enhances opportunities for land use planning and the implementation of national greenhouse gas inventories (IPCC, 2019). This approach can also enhance peatland management at more localized scales—such as individual field parcels and forest compartments—by providing detailed data on peatland extent and thickness.

5. Conclusions

New, efficient approaches are required for mapping peat extent and thickness to meet society's need to estimate and quantify atmospheric

and surface water emissions caused by peatland use. In this study, we introduced a rarely undertaken, uniquely comprehensive digital soil mapping (DSM) approach for national-scale peatland mapping utilizing machine learning (ML). The aims were to create an enhanced dataset of peat extent and thickness for Finland, assess the suitability of various data sources, conduct careful feature selection, implement independent model validation, and provide spatial estimates of prediction uncertainty. These aims were successfully achieved.

The resulting peat extent and thickness data covered all of Finland and classified peat occurrence into four categories ($\geq$10 cm, $\geq$30 cm, $\geq$40 cm, and $>$ 60 cm) with high accuracy. Comparison with legacy surficial deposit maps revealed several advantages of the developed data. The random forest (RF) predictions provided similar or higher accuracy when compared to point observations, offered more comprehensive information on peat layer thicknesses, and presented a more spatially refined depiction of peat extent. New potential peat soil areas can be identified using the proposed DSM approach. The results also complement existing peat inventory and mapping in Finland, particularly by providing data on the spatial distribution of thin peat layers ($<$10 cm), which is rarely available as continuous, uniform GIS data.

The results emphasize the importance of using a variety of features and conducting careful feature selection. Based on screening for feature collinearity, GA feature selection, and analysis of feature importance, the most influential predictors were soil wetness and terrain roughness indices derived from airborne LiDAR-based DEMs. Natural gamma radiation (potassium and thorium windows) from airborne measurements also proved highly important, with its importance increasing for the prediction of thicker peat layers ($\geq$40 cm, $>$60 cm). Additionally, optical and SAR satellite data demonstrated valuable predictive power. To our knowledge, such a comprehensive feature evaluation approach has rarely been undertaken for large-scale mapping of peat extent and thickness.

The used extensive soil observation data enabled independent model evaluation, providing a robust understanding of model performance and prediction quality. The quantified spatial variability of prediction uncertainty, in turn, offered valuable information for end users to assess the reliability of the predictions. Uncertainty was quantified through regression tree agreement and peat occurrence probability maps, allowing the evaluation of prediction uncertainty at the pixel scale. These outputs are highly useful in applications where specific types of prediction errors (e.g., Type I or Type II) are costly and must be minimized.

Overall, the results from our comprehensive DSM framework suggest that ML-based DSM approaches can enhance large-scale peatland mapping and provide improved opportunities for land use planning, nformed political steering of peatland use, and greenhouse gas inventories in alignment with national and international policies (e.g., EU Soil Strategy, EU Water Framework Directive, UNFCCC Kyoto Protocol). The predictions also support more accurate carbon stock inventories by identifying thin peat deposits and enable more localized peatland management in both agriculture and forestry.

Future research to improve the DSM of peatlands should focus on increasing the spatial resolution and expanding the peat thickness range of predictions. Key areas include ensuring the collection of up-to-date airborne datasets and peat thickness measurements across all forms of land use, enhancing the integration of time-series satellite data into the modeling process, and applying the most advanced machine learning (ML) algorithms.

CRediT authorship contribution statement

Jonne Pohjankukka: Writing – review & editing, Writing – original draft, Visualization, Validation, Software, Methodology, Formal analysis, Conceptualization. **Timo A. Räsänen:** Writing – review & editing, Writing – original draft, Visualization, Validation, Supervision, Software, Project administration, Methodology, Investigation, Funding acquisition, Formal analysis, Data curation, Conceptualization. **Timo P. Pitkänen:** Writing – review & editing, Writing – original draft, Software, Methodology, Investigation, Formal analysis, Data curation. **Arttu Kivimäki:** Writing – review & editing, Writing – original draft, Software, Investigation, Formal analysis, Data curation. **Ville Mäkinen:** Writing – review & editing, Visualization, Supervision. **Tapio Väänänen:** Writing – original draft, Investigation. **Jouni Lerssi:** Writing – original draft, Investigation. **Aura Salmivaara:** Writing – review & editing, Writing – original draft, Resources, Investigation. **Maarit Middleton:** Writing – review & editing, Writing – original draft, Validation, Supervision, Methodology, Funding acquisition, Data curation, Conceptualization.

Declaration of competing interest

The authors declare that they have no known competing financial interests or personal relationships that could have appeared to influence the work reported in this paper.

Acknowledgements

This work is part of the Advanced Spatial Data on Agricultural Peat Soils in Finland (MaaTu, 2021–2023) project funded by the Catch the Carbon program of the Ministry of Agriculture and Forestry of Finland (funding decision VN/16790/2021). The project was managed by Tapio Salo, Timo Räsänen (Luke), Tapio Kananoja (GTK), Eetu Puttonen (Finnish Geospatial Research Institute), Åke Möller (Finnish Food Authority). The authors like to acknowledge the field work crew of Joni Palola, Teuvo Herranen, Reijo Rantapelkonen, Onerva Valo, Joni Palola, Pasi Arkko, Jan Antbacka, Ville Aro (GTK) Ilkka Sarikka, Johanna Nikama and Lisa Leinonen (Luke) lead by Matti Laatikainen (GTK) and Merja Myllys (Luke). Janne Kivilompolo (GTK) compiled the reference data. Part of the predictor data preparation was funded by EU Horizon 2020 project Holisoils (Grant ID: 101000289). We made use of the high-performance computing services (Puhti) and data storage (Allas) provided by CSC – IT Center for Science (https://csc.fi/), and the geocomputing tools provided by the Open Geospatial Information Infrastructure for Research (Geoportti, urn:nbn:fi:research-infras-2016072513). Artificial intelligence tool Chat GPT 4o by Open AI (https://openai.com/) was used for proofreading the original texts written by the authors.

Appendix A

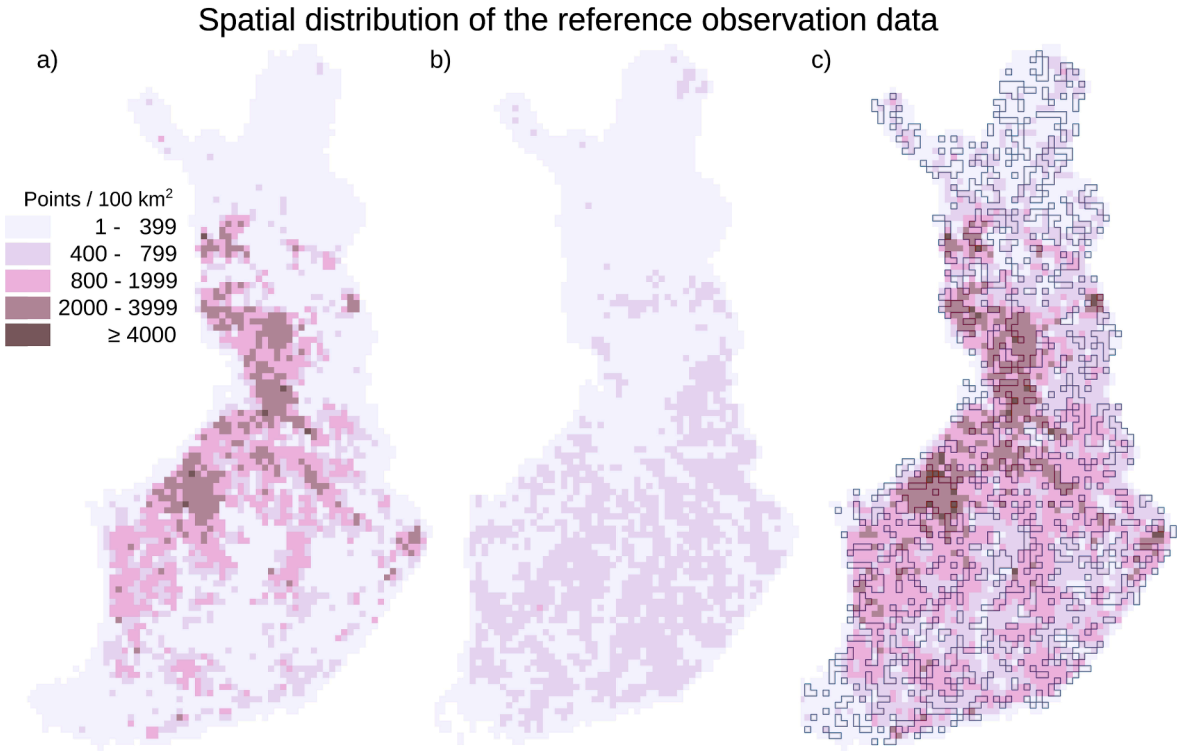

Fig. A1. The spatial distribution of the observations in the reference data used for training and testing the random forest models. The spatial distribution of the a) peat thickness measurement and soil observations, b) generated pseudo-observations, and c) the combined dataset. The points located inside the polygons in c) were used for the independent testing (30 %), the rest (70 %) were used to train models.

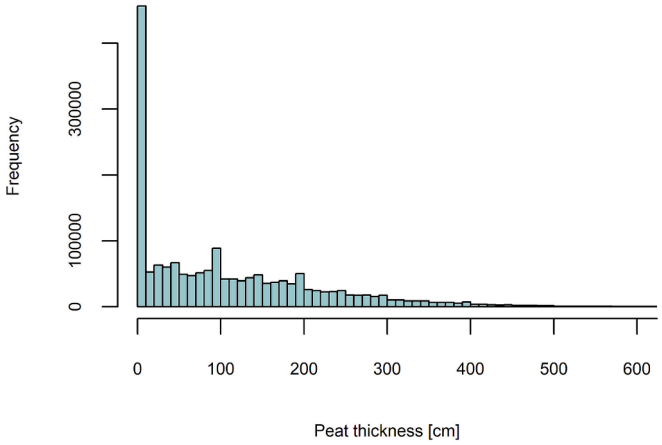

Fig. A2. Frequency histogram of all peat thickness observations (n = 1,748,580) in the reference data used for model training and testing (Table 1). Measurements larger than the upper limit of the histogram scale 600 cm are few (<0,2%). Histogram includes observations where the thickness measurement was not performed all the way to the bottom of the peat layer (<1,5%).

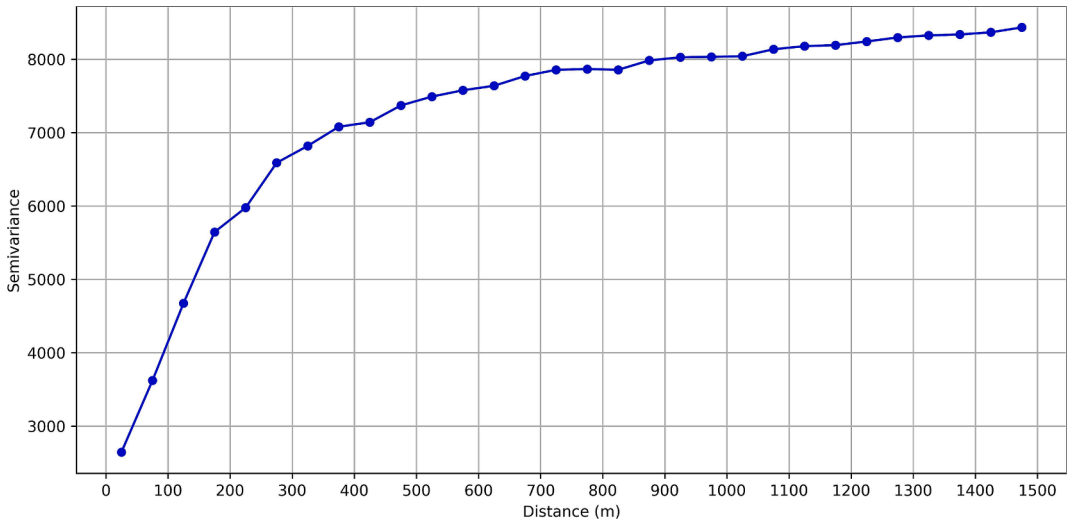

Fig. A3. Empirical omnidirectional semivariogram, calculated using observed peat depths at lag distances of 50 m.

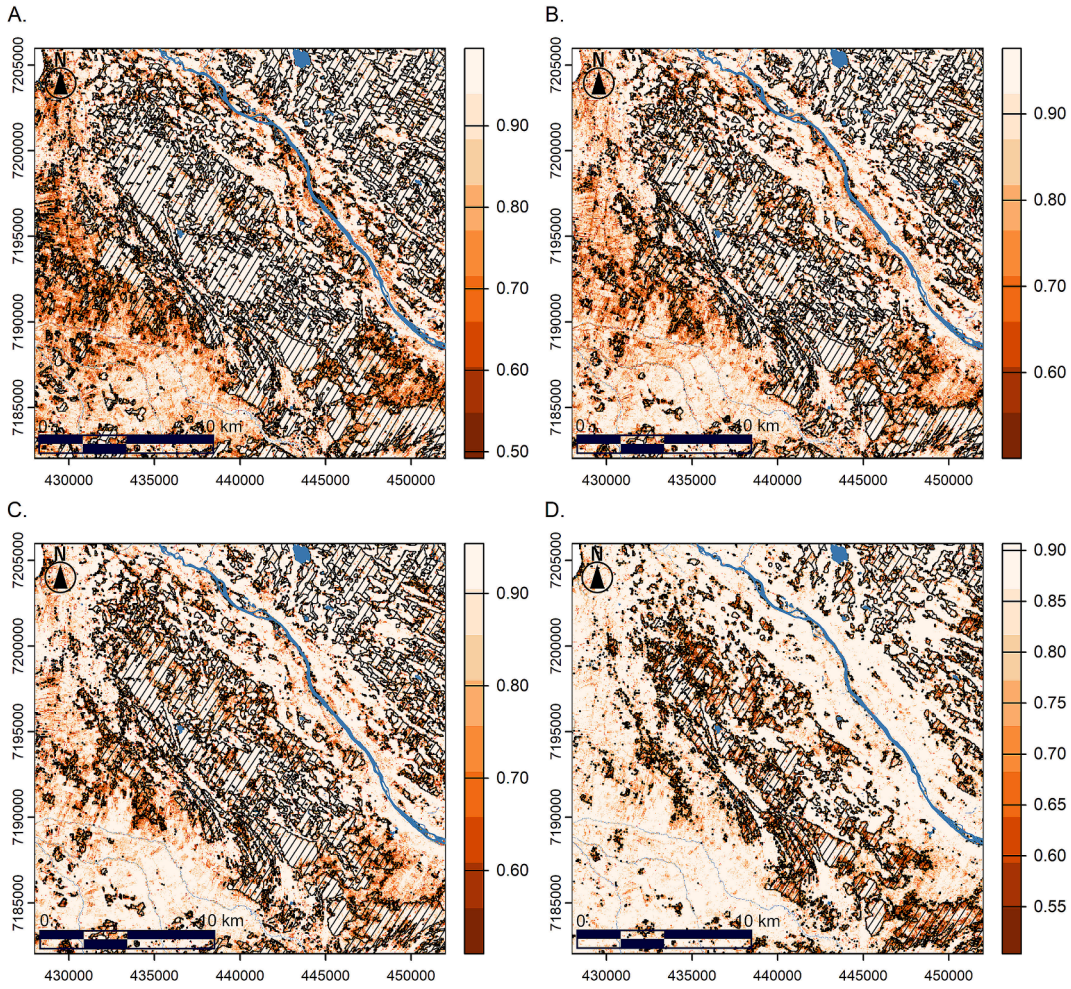

Fig. A4. Peatland classification accuracy rasters in the case of A. RF10, B. RF30, C. RF40 and, D. RF 60. The rasters are derived from the agreement rasters of Fig. 8 using the fitted polynomial functions of Fig. 9.

Table A1
Formulas for optical spectral indices. B* in formulas refer to Sentinel-2 band numbers.

Index abbreviation	Index formula
NDMI	$\frac{(B8A - B11)}{(B8A + B11)}$
NDVI	$\frac{(B8 - B4)}{(B8 + B4)}$
EVI2	$2.5 \cdot \frac{(B8 - B4)}{(2.4 \cdot B4 + B1 + 1)}$
NBR	$\frac{(B8A - B12)}{(B8A + B12)}$
kNDVI	$\tanh(NDVI^2)$
NDSI	$\frac{(B3 - B11)}{(B3 + B11)}$
SAVI	$1.5 \cdot \frac{(B8 - B4)}{(B8 + B4 + 0.5)}$
SCI	$3 \cdot B8 + B4 - B3 - 3 \cdot B2$
SM	$\frac{B8}{B2}$
TCTb	$0.3510 \cdot B2 + 0.3813 \cdot B3 + 0.3437 \cdot B4 + 0.7196 \cdot B8A + 0.2396 \cdot B11 + 0.1949 \cdot B12$
TCTg	$-0.3599 \cdot B2 - 0.3533 \cdot B3 - 0.4734 \cdot B4 + 0.6633 \cdot B8A + 0.0087 \cdot B11 + 0.2856 \cdot B12$
TCTw	$0.2578 \cdot B2 + 0.2305 \cdot B3 + 0.0883 \cdot B4 + 0.1071 \cdot B8A - 0.7611 \cdot B11 - 0.5308 \cdot B12$

Table A2
Time windows of the optical (Sentinel-2) and synthetic aperture radar (SAR; Sentinel-1) satellite mosaics.

Time windows of optical satellite mosaics	Time windows of SAR satellite mosaics
1st – 30th April 2021	1st April – 20th May 2021
15th April – 15th May 2021	
1st – 31st May 2021	
15th May – 15th June 2021	21st May – 10th July 2021
1st June – 30th June 2021	
15th June – 15th July 2021	
1st July – 31st July 2021	11th July – 31st August 2021
15th July – 15th August 2021	
1st August – 31st August 2021	
15th August – 15th September 2021	1st September – 30th November 2021
1st – 30th September 2021	
15th September – 15th October 2021	
1st – 31st October 2021	

Table A3
List of all input features to the feature selection with genetic algorithm. Yes (No) indicates if the feature was (not) selected by GA for peat predictions. Features are in alphabetical order.

Feature	Selected	Feature	Selected
AEM Im	Yes	TCTw 15th April − 15th May 2021	Yes
AR K	Yes	TCTw 1st − 31st May 2021	Yes
AR K/Th	Yes	TCTw 1st − 31st July 2021	Yes
AR Th	Yes	TCTw 15th August − 15th September 2021	Yes
DEM CVA 5x5 mean	Yes	TCTw 1st − 30th September 2021	Yes
DEM CVA 11x11 mean	Yes	AEM Re	No
DEM CVA 31x31 mean	Yes	AEM Re/Im	No
DEM CVA 5x5 std	Yes	DEM CVA 11x11 std	No
DEM CVA 31x31 std	Yes	EVI2 1st − 31st August 2021	No
DEM SAR 3x3 mean	Yes	EVI2 15th August − 15th September 2021	No
DEM SAR 3x3 std	Yes	kNDVI 1st − 31st October 2021	No
DEM slope var 31x31 mean	Yes	kNDVI 15th August − 15th September 2021	No
DEM slope var 31x31 std	Yes	NBR 1st − 31st October 2021	No
DEM var 31x31 mean	Yes	NBR 1st − 31st May 2021	No
DEM var 31x31 std	Yes	NBR 1st − 31st July 2021	No
DTW 2 ha	Yes	NBR 1st − 31st August 2021	No
EVI2 15th April − 15th May 2021	Yes	NBR 15th September − 15th October 2021	No
EVI2 1st − 31st May 2021	Yes	NDMI 1st − 31st October 2021	No
EVI2 15th May − 15th June 2021	Yes	NDMI 1st − 31st September 2021	No
EVI2 1st − 31st October 2021	Yes	NDMI 15th August − 15th September 2021	No
kNDVI 1st − 30th June 2021	Yes	NDMI 15th September − 15th October 2021	No
kNDVI 15th July − 15th August 2021	Yes	NDSI 1st − 30th April 2021	No
NBR 1st − 30th April 2021	Yes	NDSI 1st − 31st May 2021	No
NBR 15th April − 15th May 2021	Yes	NDSI 1st − 31st August 2021	No
NBR 1st − 30th June 2021	Yes	NDSI 1st − 31st September 2021	No

(*continued on next page*)

Table A3 (*continued*)

Feature	Selected	Feature	Selected
NDSI 15th April – 15th May 2021	Yes	NDSI 15th May – 15th June 2021	No
NDSI 1st – 30th June 2021	Yes	NDVI 15th September – 15th October 2021	No
NDSI 15th June – 15th July 2021	Yes	SAR Ratio 1st September – 30th November 2021	No
NDSI 1st – 31st July 2021	Yes	SAR VH 21st May – 10th July 2021	No
NDSI 15th July – 15th August 2021	Yes	SAVI 1st – 31st September 2021	No
NDSI 15th August – 15th September 2021	Yes	SAVI 1st – 31st September 2021	No
NDSI 15th September – 15th October 2021	Yes	SCI 15th September – 15th October 2021	No
NDSI 1st – 31st October 2021	Yes	SM 1st – 31st July 2021	No
NDVI 1st – 31st May 2021	Yes	SM 1st – 31st August 2021	No
NDVI 15th June – 15th July 2021	Yes	SM 15th July – 15th August 2021	No
NDVI 1st – 31st August 2021	Yes	TCTb 1st – 31st October 2021	No
NDVI 1st – 30th September 2021	Yes	TCTb 1st – 30th April 2021	No
SAVI 1st – 30th April 2021	Yes	TCTb 1st – 31st May 2021	No
SAVI 15th June – 15th July 2021	Yes	TCTb 1st – 31st August 2021	No
SAVI 1st – 31st July 2021	Yes	TCTb 15th April – 15th May 2021	No
SAVI 15th July – 15th August 2021	Yes	TCTb 15th May – 15th June 2021	No
SAR Ratio 1st April – 20th May 2021	Yes	TCTb 15th July – 15th August 2021	No
SAR Ratio 21st May – 10th July 2021	Yes	TCTb 15th August – 15th September 2021	No
SAR Ratio 11th July – 31st August 2021	Yes	TCTb 15th September – 15th October 2021	No
SAR VV 1st April – 20th May 2021	Yes	TCTg 1st – 31st October 2021	No
SAR VV 21st May – 10th July 2021	Yes	TCTg 1st – 31st May 2021	No
SAR VV 11th July – 31st August 2021	Yes	TCTg 1st – 31st August 2021	No
SAR VV 1st September – 30th November 2021	Yes	TCTg 15th May – 15th June 2021	No
SCI 1st – 31st May 2021	Yes	TCTg 15th July – 15th August 2021	No
SCI 15th May – 15th June 2021	Yes	TCTg 15th August – 15th September 2021	No
SM 15th June – 15th July 2021	Yes	TCTg 15th September – 15th October 2021	No
SM 15th August – 15th September 2021	Yes	TCTw 1st – 31st October 2021	No
Shoreline	Yes	TCTw 1st – 31st June 2021	No
TCTb 1st – 30th June 2021	Yes	TCTw 1st – 31st August 2021	No
TCTb 15th June – 15th July 2021	Yes	TCTw 15th May – 15th June 2021	No
TCTb 1st – 30th September 2021	Yes	TCTw 15th July – 15th August 2021	No
TCTg 15th June – 15th July 2021	Yes	TCTw 15th September – 15th October 2021	No
TCTg 1st – 30th September 2021	Yes		
TCTw 1st – 30th April 2021	Yes		

Data availability

The authors do not have permission to share data.

References

Abu-Mostafa, Y.S., Magdon-Ismail, M., Lin, H.-T., 2012. Learning from Data: Amlbook.

Ågren, A.M., Lidberg, W., Stromgren, M., Ogilvie, J., Arp, P.A., 2014. Evaluating digital terrain indices for soil wetness mapping – a Swedish case Study. Hydrol. Earth Syst. Sc. 18, 3623–3634. https://doi.org/10.5194/hess-18-3623-2014.

Ågren, A.M., Larson, J., Paul, S.S., Laudon, H., Lidberg, W., 2021. Use of multiple LIDAR-derived digital terrain indices and machine learning for high-resolution national-scale soil moisture mapping of the Swedish forest landscape. Geoderma 404, 115280. https://doi.org/10.1016/j.geoderma.2021.115280.

Ågren, A.M., Hasselquist, E.M., Stendahl, J., Nilsson, M.B., Paul, S.S., 2022. Delineating the distribution of mineral and peat soils at the landscape scale in northern boreal regions. SOIL 8, 733–749. https://doi.org/10.5194/soil-8-733-2022.

Airo, M., Hyvönen, E., Lerssi, J., Leväniemi, H., Ruotsalainen, A., 2014. Tips and tools for the application of GTK's airborne geophysical data. GTK Report of Investigation 215. accessed 20 May 2023 Geological Survey of Finland. 33, p. http://tupa.gtk.fi/julkaisu/tutkimusraportti/tr_215.pdf.

Airo, M., (ed.), 2005. Aerogeophysics in Finland 1972-2004: Methods, System Characteristics and Applications. Geological Survey of Finland, Special Paper 39. 197 p., 8 apps. Available: https://tupa.gtk.fi/julkaisu/specialpaper/sp_039.pdf (accessed 20 May 2023).

Aitkenhead, M.J., 2017. Mapping peat in Scotland with remote sensing and site characteristics. Eur. J. Soil. Sci. 68, 28–38. https://doi.org/10.1111/ejss.12393.

Alalammi, P. (Ed.), 1986. Atlas of Finland. Folio 121-122. Relief and Landforms. Publishers: National Board of Survey, Geographical Society of Finland.

Antropov, O., Rauste, Y., Astola, H., Praks, J., Häme, T., Hallikainen, M.T., 2014. Land Cover and Soil Type Mapping from Spaceborne PolSAR Data at L-Band with Probabilistic Neural Network,". IEEE Trans. Geosci. Remote Sens. 52 (9), 5256–5270. https://doi.org/10.1109/TGRS.2013.2287712.

Beamish, D., 2015. Relationships between gamma-ray attenuation and soils in SW England. Geoderma 259–260 (2015), 174–186. https://doi.org/10.1016/j.geoderma.2015.05.018.

Bhiry, N., Payette, S., Robert, E.C., 2007. Peatland development at the arctic tree line (Québec, Canada) influenced by flooding and permafrost. Quat. Res. 67 (3), 426–437. https://doi.org/10.1016/j.yqres.2006.11.009.

Bishop, C. M., Bishop, H. & Cham, S. (ed.) (2023). Deep Learning – Foundations and Concepts. ISBN: 978-3-031-45468-4.

Breiman, L., 2001. Random Forests. Mach. Learn. 45, 5–32. https://doi.org/10.1023/A:1010933404324.

Bruneau P. M. C., Johnson S. M., 2014. Scotland's Peatland-Definitions & Information Resources; Scottish Natural Heritage Commissioned Report, No. 701, Scottish Natural Heritage, Edinburgh, UK.

Camps-Valls, G., Campos-Taberner, M., Moreno-Martínez, Á., Walther, S., Duveiller, G., Ces-catti, A., Mahecha, M.D., Muñoz-Marí, J., García-Haro, F.J., Guanter, L., Jung, M., Gamon, J.A., Reichstein, M., Running, S.W., 2021. A unified vegetation index for quantifying the terrestrial biosphere. Sci. Adv. 7 (9), eabc7447. https://doi.org/10.1126/sciadv.abc7447.

Chen, R., C., Dewi, C., Huang, S. W., 2020. Selecting critical features for data classification based on machine learning methods. J. Big Data, 7, 52. doi: 10.1186/s40537-020-00327-4.

Davisson, C. M. (1968). Interaction of gamma-radiation with matter. In: Sieg-bahn, K. (ed.), Alpha-, Beta- and Gamma-ray Spectroscopy, p. 37–78, ISBN: 9780444596994.

DeLancey E., R., Kariyeva J., Bried J. T., Hird J. N., 2019. Large-scale probabilistic identification of boreal peatlands using Google Earth Engine, open-access satellite data, and machine learning. PLoS ONE 14, 6, e0218165. doi: 10.1371/journal.pone.0218165.

Dupigny-Giroux, L.-A., Lewis, J.E., 1999. A Moisture lndex for Surface Characterization over a Semiarid Area. Photogramm. Eng. Remote Sens. 65 (8), 937–945.

Endrestøl, G.O., 1980. Principle and method for measurement of snow water equivalent by detection of natural gamma radiation / Principe et méthode pour la mesure de l'hauteur d'eau équivalente par détection du rayonnement gamma naturel. Hydrol. Sci. Bull. 25 (1), 77–83. https://doi.org/10.1080/02626668009491906.

Esa, 2024a. SENTINEL-2 MSI Technical Guide. Sentinel Online, European space Agency https://sentinels.copernicus.eu/web/sentinel/technical-guides/sentinel-2-msi, (accessed 14 April 2024.

Esa, 2024b. Sentinel-1 SAR Technical Guide. Sentinel Online, European space Agency https://sentinels.copernicus.eu/web/sentinel/technical-guides/sentinel-1-sar (accessed 14. April 2024.

Eurola, S., Huttunen, A. & Kukko-Oja, K. 1994. Suokasvillisuus. Oulanka reports 13. Oulangan tutkimusasema, Oulun yliopisto.

European Commission, 2021. EU Soil Strategy for 2030: Reaping the benefits of healthy soils for people, food, nature, and climate (COM(2021) 699 final). Accessed 4 Jan 2025. https://environment.ec.europa.eu/document/download/ae853f10-c9a2-4665-a9f2-c29d11c49374_en?filename=COM_2021_699_1_EN_ACT_part1_v4_0.pdf.

Evans, C.D., Peacock, M., Baird, A.J., Artz, R.R.E., Burden, A., Callaghan, N., Chapman, P.J., Cooper, H.M., Coyle, M., Craig, E., Cumming, A., Dixon, S., Gauci, V., Grayson, R.P., Helfter, C., Heppell, C.M., Holden, J., Jones, D.L., Kaduk, J., Levy, P.,

Matthews, R., McNamara, N.P., Misselbrook, T., Oakley, S., Page, S.E., Rayment, M., Ridley, L.M., Stan-ley, K.M., Williamson, J.L., Worrall, F., Morrison, R., 2021. Overriding water table control on managed peatland greenhouse gas emissions. Nature 1–5. https://doi.org/10.1038/s41586-021-03523-1.

Fadhurrahman, M., Saputro, A.H., 2022. Peat Depth Prediction System Using Long-Term MODIS Data and Random Forest Algorithm: A Case Study in Pulang Pisau, Kalimantan. 1st International Conference on Information System & Information Technology (ICISIT), Yogyakarta, Indonesia, 2022, pp. 364-369. https://10.1109/ICISIT54091.2022.9872550.

Farahnakian, F., Pohjankukka, J., Zelioli., L., Farahnakian, F., Pitkänen, T., Tuominen, S., Balazs, A., Heikkonen, J., Middleton, M., *in prep*. Classifying Boreal Peatlands with Remote Sensing and Machine Learning: Methodological Comparison for Country-Wide Mapping.

Fawcett, T., 2006. An introduction to ROC analysis. Pattern Recogn. Lett. 27 (8), 861–874. https://doi.org/10.1016/j.patrec.2005.10.0101027.

Fernandez-Ugalde, O., Scarpa, S., Orgiazzi, A., Panagos, P., van Liedekerke, M., Maréchal, A., Jones, A., 2022. LUCAS 2018 Soil Module (JRC Technical Reports). European Commission, Joint Research Centre (JRC) http://doi:10.2760/215013.

Fluet-Chouinard, E., Stocker, B.D., Zhang, Z., 2023. Extensive global wetland loss over the past three centuries. Nature 614, 281–286. https://doi.org/10.1038/s41586-022-05572-6.

FMI, 2020. Sentinel-1 SAR-image mosaic (S1sar). Finnish Meteorological Institute. https://ckan.ymparisto.fi/dataset/sentinel-1-sar-image-mosaic-s1sar-sentinel-1-sar-kuvamosaiikki-s1sar (accessed 17 April 2024).

Gao, B., 1996. NDWI—A normalized difference water index for remote sensing of vegetation liquid water from space. Remote Sens. Environ. 58 (3), 257–266. https://doi.org/10.1016/S0034-4257(96)00067-3.

Gatis, N., Luscombe, D.J., Carless, D., Parry, L.E., Fyfe, R.M., Harrod, T.R., Brazier, R.E., Anderson, K., 2019. Mapping upland peat depth using airborne radiometric and lidar survey data. *Geoderma* 335, 78–87. https://doi.org/10.1016/j.geoderma.2018.07.041.

Goutte, C., Gaussier, E., 2005. A Probabilistic Interpretation of Precision, Recall and F-Score, with Implications for Evaluation. In: Losada, D.E., Fernández-Luna, J.M. (Eds.), Advances in Information Retrieval. Springer, Berlin Heidelberg, Berlin, Heidelberg, pp. 345–359. https://doi.org/10.1007/978-3-540-31865-1_25.

Grønlund, A., Hauge, A., Hovde, A., Rasse, D.P., 2008. Carbon loss estimates from cultivated peat soils in Norway: a comparison of three methods. Nutr. Cycl. Agroecosyst. 81, 157–167. https://doi.org/10.1007/s10705-008-9171-5.

GTK 2010, Superficial deposits of Finland 1:200,000 [data]. Geological Survey of Finland (GTK). http://hakku.gtk.fi (accessed 26. Feb 2024).

GTK, 2013. Ancient shorelines [data]. Geological Survey of Finland (GTK). http://hakku.gtk.fi (accessed 26. Apr 2024).

GTK 2015b. Superficial deposits 1:100 000 [data]. Geological Survey of Finland (GTK). http://hakku.gtk.fi (accessed 26. Feb 2024).

GTK, 2017. Investigated peatland areas [data]. Geological Survey of Finland (GTK). http://hakku.gtk.fi (accessed 26. Feb 2024).

GTK, 2017. Acid sulfate soils 1:250 000 [data]. Geological Survey of Finland (GTK). http://hakku.gtk.fi, (accessed 26. Feb 2024).

GTK, 2018. Stratum data for superficial deposits [data]. Geological Survey of Finland (GTK). http://hakku.gtk.fi (accessed 26. Feb 2024).

Haavisto, M. (editor) 1983. Maaperäkartan käyttöopas 1:20,000, 1:50,000. Summary: Basic Mapping of Quaternary Deposits in Finland. Geological Survey of Finland, Guide 10. 80 pages, Maanmittauslaitoksen kirjapaino, Helsinki. ISBN 951-690-170-0.

Gtk, 2015. Superficial deposits 1. 000 [data]. Geological Survey of Finland (GTK) 20 ,000/1:, 50 accessed 26. Feb 2024.

Hastie, T., Tibshirani, R., Friedman, J., 2001. The Elements of Statistical Learning. NY, USA, Springer, New York Inc, New York.

Heikkinen, J., Keskinen, R., Regina, K., Honkanen, H., Nuutinen, V., 2021. Estimation of carbon stocks in boreal cropland soils - methodological considerations. Eur. J. Soil Sci. 72, 934–945. https://doi.org/10.1111/ejss.13033.

Hird, J.N., DeLancey, E.R., McDermid, G.J., Kariyeva, J., 2017. Google Earth Engine, Open-Access Satellite Data, and Machine Learning in Support of Large-Area Probabilistic Wetland Mapping. Remote Sens. 9, 1315. https://doi.org/10.3390/rs9121315.

Hokkanen, K.,2005. Lounais-Hämeen muinaisranta-analyysit ja muinaisrantojen visualisointi (Analysis and Visualization of Ancient Shorelines in Southwestern Häme, Finland). Report p.22.4.110. Geological Survey of Finland. http://tupa.gtk.fi (accessed 20 May 2024).

Huete, A.R., 1988. A soil-adjusted vegetation index (SAVI). Remote Sens. Environ. 25 (3), 295–309. https://doi.org/10.1016/0034-4257(88)90106-X.

Hyvönen, E., Turunen, P., Vanhanen, E., Arkimaa, H., Sutinen, R., 2005. Airborne gamma-ray surveys in Finland. In: Airo, M-L. (ed.), Aerogeophysics in Finland 1972-2004; Methods, system characteristics and application. Geological Survey of Finland, Special Paper 39, 119-134. https://tupa.gtk.fi/ (accessed 26. Feb 2024).

Iaea, 1991. Airborne gamma ray spectrometer surveying. International Atomic Energy Agency, Technical Report Series, No, p. 323.

IPCC, 2019. Refinement to the 2006 IPCC Guidelines for National Greenhouse Gas Inventories, Calvo Buendia, E., Tanabe, K., Kranjc, A., Baasansuren, J., Fukuda, M., Ngarize, S., Osako, A., Pyrozhenko, Y., Shermanau, P. and Federici, S. (eds). IPCC, Switzerland.

Ips, 2024. What is peat? International Peatland Society. accessed 27. Feb 2024. https://peatlands.org.

IUSS Working Group WRB, 2022. World Reference Base for Soil Resources. International soil classification system for naming soils and creating legends for soil maps, 4th edition. International Union of Soil Sciences (IUSS), Vienna, Austria.

Jenny, H., 1994. Factors of soil formation: a system of quantitative pedology. Dover Publications Inc., New York, p. 281.

Jones, A., Fernandez-Ugalde, O. & Scarpa, S. 2020. LUCAS 2015 Topsoil Survey, Presentation of dataset and results. JRC Technical Reports. 83 p. European Commission Joint Re-search Centre (JRC). http://doi:10.2760/616084.

Karasiak, N., Dejoux, J.F., Monteil, C., Sheenen, D., 2022. Spatial dependence between training and test sets: another pitfall of classification accuracy assessment in remote sensing. Mach. Learn. 111, 2715–2740. https://doi.org/10.1007/s10994-021-05972-1.

Karlson, M., Bastviken, D., 2023. Multi-source mapping of peatland types using Sentinel-1, Sentinel-2, and terrain derivatives—A comparison between five high-latitude landscapes. J. Geophys. Res. Biogeo. 128, e2022JG007195. https://doi.org/10.1029/2022JG007195.

Kaur, H., Pannu, H.S., Malhi, A.K., 2019. A Systematic Review on Imbalanced Data Challenges in Machine Learning: Applications and Solutions. ACM Comput. Surv. 52, 4, 79, 1–36. https://doi.org/10.1145/3343440.

Kauth, R., Thomas, G., 1976. The tasseled Cap—A Graphic Description of the Spectral-Temporal Development of Agricultural Crops as Seen by LANDSAT. accessed 26. Feb 2024 LARS Symposia 159. https://docs.lib.purdue.edu/lars_symp/159/.

Key, C., Benson N. 1999. Measuring and remote sensing of burn severity: The CBI and NBR. Poster abstract. Proceedings Joint Fire Science Conference and Workshop Vol. II: 284.

Korhonen, K.T., Ahola, A., Heikkinen, J., Henttonen, H.M., Hotanen, J.-P., Ihalainen, A., Melin, M., Pitkänen, J., Räty, M., Sirviö, M., Strandström, M., 2021. Forests of Finland 2014–2018 and their development 1921–2018. Silva Fenn. 55 (5), 10662. https://doi.org/10.14214/sf.10662.

Korpela, I., Haapanen, R., Korrensalo, A., Tuittila, E.-S., Vesala, T., 2020. Fine-resolution mapping of microforms on a boreal bog using aerial images and waveform-recording LiDAR. Mire Peat. https://doi.org/10.19189/MaP.2018.OMB.388.

Laatikainen, M., Leino, J., Lerssi, J., Torppa, J. & Turunen, J. 2011. Turvetutkimusten menetelmäkehitystarkastelu - A new approach for peat inventory methods. Report of peat investigation 414, Geological Survey of Finland, 134 pages, 150 figures and 5 tables. Available at: https://tupa.gtk.fi/raportti/turve/ttr_414.pdf.

Lahti, K., Häme, T., 1992. Discrimination of peatlands and mineral soil lands using multisource remote sensing data. In: International Society for Photogrammetry and Remote Sensing XVIth Congress, Washington D.C., 452–456.

Lerssi, J., Säävuori, H., & Nousiainen, M., 2023. Turpeen paksuuden arviointi geofysikaalisten lentomittausten perusteella (Estimating peat thickness based on airborne geophysical surveys). Research report, 74, Geological Survey of Finland (GTK). https://tupa.gtk.fi/ (accessed 27. Feb 2024).

Lappalainen, E., Stén, C.-G., Häikiö, J., 1984. Turvetutkimusten maasto-opas. Geologian Tutkimuskeskus, Opas 12, 62 p. https://tupa.gtk.fi/julkaisu/opas/op_012.pdf.

Lidberg, W., Nilsson, M., Ågren, A., 2020. Using machine learning to generate high-resolution wet area maps for planning forest management: A study in a boreal forest landscape. Ambio 49, 475–486. https://doi.org/10.1007/s13280-019-01196-9.

Lilja, H., Uusitalo, R., Yli-Halla, M., Nevalainen, R., Väänänen, R., Tamminen, P., Tuhtar, J., 2017. Suomen maannostietokanta: Käyttöopas versio 1.1 (Finnish Soil Database: Manual, version 1.1). Luonnonvara- ja biotalouden tutkimus. Natural Resources Institute Finland (Luke). http://urn.fi/URN:ISBN:978-952-326-357-4 (accessed 25. May 2024).

Loecher, M., Lai, D., Qi, W., 2022. Approximation of SHAP Values for Randomized Tree Ensembles. In: Holzinger, A., Kieseberg, P., Tjoa, A.M., Weippl, E. (eds), Machine Learning and Knowledge Extraction. CD-MAKE 2022. Lecture Notes in Computer Science, vol 13480. Springer, Cham. doi: 10.1007/978-3-031-14463-9_2.

Lundberg, S.M., Erion, G., Chen, H., et al., 2020. From local explanations to global understanding with explainable AI for trees. Nat Mach Intell 2, 56–67. https://doi.org/10.1038/s42256-019-0138-9.

Mäkilä, M., Säävuori, H., Kuznetsov, O. & Grundström, A., 2013. Soiden ikä ja kehitys Suomessa (Age and development of mires in Finland). Turvetutkimusraportti 443, Geologian tutkimuskeskus (Geological Survey of Finland). https://tupa.gtk.fi/ (accessed 20 May 2024).

Melton, J.R., Chan, E., Millard, K., Fortier, M., Winton, R.S., Martín-López, J.M., Cadillo-Quiroz, H., Kidd, D., Verchot, L.V., 2022. A map of global peatland extent created using machine learning (Peat-ML). Geosci. Model Dev. 15, 4709–4738. https://doi.org/10.5194/gmd-15-4709-2022.

Metsäntutkimuslaitos 2009. Valtakunnallinen metsien 11. Inventointi (VMI 11), Maastotyön ohjeet 2009. Koko Suomi. 2. painos. Metsäntutkimuslaitos, Vantaa 2009. 150 p.

Minasny, B., Adetsu, D.V., Aitkenhead, M., et al., 2024. Mapping and monitoring peatland conditions from global to field scale. *Biogeochemistry* 167, 383–425. https://doi.org/10.1007/s10533-023-01084-1.

Minasny, B., Berglund, Ö., Connolly, J., Hedley, C., de Vries, F., Gimona, A., Kempen, B., Kidd, D., Lilja, H., Malone, B., McBratney, A., Roudier, P., O'Rourke, S., Rudiyanto, Padarian, J., Poggio, L., ten Caten, A., Thompson, D., Tuve, C., & Widyatmanti, W., 2019. Digital mapping of peatlands – A critical review. Earth-Science Reviews, 196, 102870. doi: 10.1016/j.earscirev.2019.05.014.

Murphy, P., Ogilvie, J., Connor, K., Arp, P., 2007. Mapping wetlands: A comparison of two different approaches for New Brunswick, Canada. Wetlands 27, 846–854. https://doi.org/10.1672/0277-5212(2007)27[846:MWACOT]2.0.CO;2.

Murphy, P., Ogilvie, J., Castonguay, M., Zhang, C., Meng, F.R., Arp, P., 2008. Improving forest operations planning through high-resolution flow-channel and wet-areas mapping. Forestry Chron. 84, 568–574. https://doi.org/10.5558/tfc84568-4.

Nielsen, F., 2016. Hierarchical Clustering. In: Introduction to HPC with MPI for Data Science. Undergraduate Topics in Computer Science. Springer, Cham. https://doi.org/10.1007/978-3-319-21903-5_8.

NLS, 2020. Elevation model 2 m [WWW Document]. National Land Survey of Finland. URL https://www.maanmittauslaitos.fi/en/maps-and-spatial-data/expert-users/product-descriptions/elevation-model-2-m (accessed 22 Mar 2024).
NLS, 2024.Topographic Database 1:10 000 [data]. National Land Survey of Finland. https://www.maanmittauslaitos.fi/en/maps-and-spatial-data/datasets-and-interfaces/product-descriptions/topographic-database (accessed 26. Feb 2024).
O'Leary, D., Brown, C., Daly, E., 2022. Digital soil mapping of peatland using airborne radiometric data and supervised machine learning – Implication for the assessment of carbon stock. Geoderma 428 (2022), 116086. https://doi.org/10.1016/j.geoderma.2022.116086.
O'Leary, D., Brown, C., Hodgson, J., Connolly, J., Gilet, L., Tuohy, P., Fenton, O., Daly, E., 2025. Airborne radiometric data for digital soil mapping of peat at broad and local scales. Geoderma 453 (2025), 117129. https://doi.org/10.1016/j.geoderma.2024.117129.
Oshiro, T.M., Perez, P.S., Baranauskas, J.A., 2012. How Many Trees in a Random Forest?. In: Perner, P. (eds) Machine Learning and Data Mining in Pattern Recognition. MLDM 2012. Lecture Notes in Computer Science, vol 7376. Springer, Berlin, Heidelberg. doi: 10.1007/978-3-642-31537-4_13.
Padarian, J., McBratney, A.B., Minasny, B., 2020. Game theory interpretation of digital soil mapping convolutional neural networks. *SOIL* 6 (2), 389–397. https://doi.org/10.5194/soil-6-389-2020.
Päivänen, J., 1973. Hydraulic conductivity and water retention in peat soils. Acta Forestalia Fennica 129, 7563. https://doi.org/10.14214/aff.7563.
European Parliament and Council, 2000. Directive 2000/60/EC of the European Parliament and of the Council of 23 October 2000 establishing a framework for Community action in the field of water policy. Official Journal of the European Communities, L 327, 1–73. https://eur-lex.europa.eu/eli/dir/2000/60/oj Accessed 4 Jan 2025.
Pedregosa, et al., 2011. Scikit-learn: Machine Learning in Python. J. Mach. Learn. Res. 12 (85), 2825–2830.
Pittman, R. and Hu, B., 2022. Improving the binary classification of peat localities from multi-source remotely-sensed data using CNN, Int. Arch. Photogramm. Remote Sens. Spatial Inf. Sci., XLIII-B3-2022, 983–988, doi: 10.5194/isprs-archives-XLIII-B3-2022-983-2022.
Poggio, L., Lassauce, A., Gimona, A., 2019. Modelling the extent of northern peat soil and its uncertainty with Sentinel: Scotland as example of highly cloudy region. Geoderma 346 (2019), 63–74. https://doi.org/10.1016/j.geoderma.2019.03.017.
Pohjarakennuksen normit 1964. Rakennusinsinööriliiton julkaisuja, Sarja A, 45. Helsinki: Rakennusinsinöörien liitto. 38 p.
Puranen, R., Säävuori, H., Sahala, I., Suppala, I., Mäkilä, M., Lerssi, J., 1999. Airborne electromagnetic mapping of surficial deposits in Finland. First Break 17 (5), 145–154. https://doi.org/10.1046/j.1365-2397.1999.00704.x.
Räsänen, T.A., Myllys, M., Kekkonen, H., Salo., T., Pitkänen, T., Laatikainen, M. Laine-Petäjäkangas, A., Väänänen, T., Palmu, J.-P., Kivimäki, A. & Oksanen J. 2023. Turvepeltolohkojen määrittely ja tunnistaminen: Maatalousmaiden turvetieto (MaaTu) -hankkeen raportti (Definition and identification of field parcels with peat – A report of Advanced Spatial data on Agricultural Peat Soils project). Luonnonvara- ja biotalouden tutkimus, 58/2023. Natural Resources Institute Finland (Luke). Helsinki. http://urn.fi/URN:ISBN:978-952-380-720-4 (accessed 20 May 2024).
Reinhardt, N., Herrmann, L., 2019. Gamma-ray spectrometry as versatile tool in soil science: A critical review. J. Plant Nutr. Soil Sci. 182, 9–27. https://doi.org/10.1002/jpln.201700447.
Riggs, G. A., Hall, D. K., Salomonson, V. V., 1994. A snow index for the Landsat Thematic Map-per and Moderate Resolution Imaging Spectroradiometer. Proceedings of IGARSS '94 - 1994 IEEE International Geoscience and Remote Sensing Symposium 4, 1942–1944. doi: 10.1109/IGARSS.1994.399618.
Rimondini, L., Gumbricht, T., Ahlström, A., Hugelius, G., 2023. Mapping of peatlands in the forested landscape of Sweden using LiDAR-based terrain indices. Earth Syst. Sci. Data Discuss. 2023, 1–17. https://doi.org/10.5194/essd-15-3473-2023.
Rouse, J.W., Haas, R.H., Schell, J.A., Deering, D.W., 1973. Monitoring Vegetation Systems in the Great Plains with ERTS (Earth Resources Technology Satellite). Proceedings of 3rd Earth Resources Technology Satellite Symposium.
Ruuhijärvi, R., 1988. Suokasvillisuus. – Suomen kartasto 141–143, s. 2-6. Maanmittaushallitus & Suomen maantieteellinen seura, Helsinki.
Salmivaara, A., 2023. Cartographic Depth-to-Water (DTW) index map, 2m [data]. CSC – IT Center for Science. http://urn.fi/urn:nbn:fi:att:770f345e-58d4-45e5-b4e7-3fdbd858872f (accessed 20 May 2024).
Sastry, K., Goldberg, D., Kendall, G., 2005. Genetic Algorithms. In: Burke, E.K., Kendall, G. (Eds.), Search Methodologies. Springer, Boston, MA. https://doi.org/10.1007/0-387-28356-0_4.
Schnug, E., Haneklaus, S., Schnier, C., Scholten, L.C., 1996. Issues of natural radioactivity in phosphates. Commun. Soil Sci. Plant Anal. 27 (3–4), 829–841. https://doi.org/10.1080/00103629609369600.
sen2mosaic, 2017. Documentation for SMFM sen2mosaic. https://sen2mosaic.readthedocs.io (accessed 17 Apr 2024).
Shannon, C.E., 1948. A Mathematical Theory of Communication. Bell Syst. Tech. J. 27, 379–423. https://doi.org/10.1002/j.1538-7305.1948.tb01338.x.
Shi, T., Xu, H., 2019. Derivation of Tasseled Cap Transformation Coefficients for Sentinel-2 MSI At-Sensor Reflectance Data. IEEE J. Sel. Top. Appl. Earth Obs. Remote Sens. 12 (10), 4038–4048. https://doi.org/10.1109/JSTARS.2019.2938388.
Shimada, S., Takada, M., Takahashi, H., 2016. Peat Mapping. In: Osaki, M., Tsuji, N. (Eds.), Tropical Peatland Ecosystems. Springer, Tokyo. https://doi.org/10.1007/978-4-431-55681-7_31.
Siemon, B., Ibs-von Seht, M., Frank, S., 2020. Airborne Electromagnetic and Radiometric Peat Thickness Mapping of a Bog in Northwest Germany (Ahlen-Falkenberger Moor). Remote Sens. (Basel) 12, 2. https://doi.org/10.3390/rs12020203.
Silvestri, S., Christensen, C.W., Lysdahl, A.O.K., Anschütz, H., Pfaffhuber, A.A., Viezzoli, A., 2019. Peatland volume mapping over resistive substrates with airborne electromagnetic technology. Geophys. Res. Lett. 46, 6459–6468. https://doi.org/10.1029/2019GL083025.
Soinne, H., Kurkilahti, M., Heikkinen, J., Eurola, M., Uusitalo, R., Nuutinen, V., Keskinen, R., 2022. Decadal trends in soil and grain microelement concentrations indicate mainly favourable development in Finland. J. Plant Nutr. Soil Sci. 185, 578–588. https://doi.org/10.1002/jpln.202200141.
Statistics Finland, 2025. Environment and nature. Available: https://stat.fi/tup/suoluk/suoluk_alue_en.html (Accessed 5.2.2025).
Štrumbelj, E., Kononenko, I., 2014. Explaining prediction models and individual predictions with feature contributions. Knowl. Inf. Syst. 41, 647–665. https://doi.org/10.1007/s10115-013-0679-x.
Suppala, I., Oksama, M., Hongisto, H., 2005. GTK airborne EM system: Characteristics and interpretation guidelines. In: Airo, M-L. (ed.), Aerogeophysics in Finland 1972-2004; Methods, system characteristics and application. Geological Survey of Finland, Special Paper 39, 103-118. https://tupa.gtk.fi/ (accessed 20 May 2024).
Syke, 2024. Suokasvillisuusvyöhykkeet. Mire vegetation zones. (CC BY 4.0).
Syke, 2024. Metsäkasvillisuusvyöhykkeet. Climate driven forest vegetation zones. (CC BY 4.0).
Tanneberger, F., Tegetmeyer, C., Busse, S., Barthelmes, A., Shumka, S., Moles Mariné, A., Jenderedjian, K., Steiner, G.M., Essl, F., Etzold, J., Mendes, C., Kozulin, A., Frankard, P., Milanović, D., Ganeva, A., Apostolova, I., Alegro, A., Delipetrou, P., Navrátilová, J., Risager, M., Leivits, A., Fosaa, A.M., Tuominen, S., Muller, F., Bakuradze, T., Sommer, M., Christanis, K., Szurdoki, E., Oskarsson, H., Brink, S.H., Connolly, J., Bragazza, L., Martinelli, G., Aleksāns, O., Priede, A., Sungaila, D., Melovski, L., Belous, T., Saveljić, D., deVries, F., Moen, A., Dembek, W., Mateus, J., Hanganu, J., Sirin, A., Markina, A., Napreenko, M., Lazarević, P., Šefferová Stanová, V., Skoberne, P., Heras Pérez, P., Pontevedra-Pombal, X., Lonnstad, J., Küchler, M., Wüst-Galley, C., Kirca, S., Mykytiuk, O., Lindsay, R., Joosten, H., 2017. The peatland map of Europe. Mire Peat 19 (22), 1–17. http://doi.org/10.19189/MaP.2016.OMB.264.
Tóth, G., Jones, A., Montanarella, L., 2013. LUCAS Topsoil Survey. Methodology, data and results. JRC Technical Reports. Scientific and Technical Research Series. https://doi.org/10.2788/97922.
Turunen, J., Valpola, S., 2020. The influence of anthropogenic land use on Finnish peatland area and carbon stores 1950–2015. Mire Peat 26, 26. https://doi.org/10.19189/MaP.2019.GDC.StA.1870.
Uddin, S., Khan, A., Hossain, M., et al., 2019. Comparing different supervised machine learning algorithms for disease prediction. BMC Med Inform Decis Mak 19, 281. https://doi.org/10.1186/s12911-019-1004-8.
Tikkanen, M., Oksanen, J., 2002. Late Weichselian and Holocene shore displacement history of the Baltic Sea in Finland. Fennia 180: 1–2, pp. 9–20. Helsinki. ISSN 0015-0010.
Virtanen, K., 1997. Lentomittausten gamma-aineisto – Menetelmä arvioida turvekerrostumien paksuutta (Airborne Gamma-Ray Survey Data – A Method to Assess the Thickness of Peat Layers). Suo Ja Turve 397, 97.
Virtanen, K., Hänninen, P., Kallinen, R.-L., Vartiainen, S., Herranen, T., Jokisaari, R., 2003. The peat reserves of Finland in 2000. Geological Survey of Finland. Report of Investigation 156, 101 p. https://tupa.gtk.fi/julkaisu/tutkimusraportti/tr_156.pdf.
Wadoux, A.-M.-J.-C., Minasny, B., McBratney, A.B., 2020. Machine learning for digital soil mapping: Applications, challenges, and suggested solutions. Earth-Sci. Rev. 210, 103359. https://doi.org/10.1016/j.earscirev.2020.103359.
Wold, S., Esbensen, K., Geladi, P., 1987. Principal Component Analysis. Chemom. Intel. Lab. Syst. 2 (1–3), 37–52. https://doi.org/10.1016/0169-7439(87)80084-9.
Yli-Halla, M., Talkkari, A., Nyholm, R., Nevalainen, R., Lerssi, J., Väänänen, T., Tamminen, P., Starr, M., 2003. Numeerinen Suomen maannostietokanta mittakaavassa 1:250 000-pilottihanke (Georeferenced Soil Database of Finland at Scale 1:250,000 - Pilot project). Mtt:n Selvityksiä 44, 52 p.